Eidgenössische Technische Hochschule Zürich
Swiss Federal Institute of Technology Zurich

Towards the Realisation of Transport Entangling Gates with Trapped Ions

Master's Thesis of	:	Paolo Colciaghi
Supervisor	:	Matteo Marinelli
Professor	:	Jonathan P. Home

October 2018

Abstract

Over the last few decades trapped ions have proven to be one of the most promising implementations of quantum information processing (QIP), as all necessary fundamental operations have been demonstrated with sufficient fidelity. Nevertheless, the scalability of the apparatus to a many-qubit device still represents a major challenge, since at the moment several square metres of optics and electronics are needed for the control of a few ions.

This thesis stands exactly in this perspective, in that it aims to the production of high-fidelity entangling gates according to a more scalable working principle. Indeed, in this text are presented the theoretical and experimental efforts towards the production of transport Mølmer Sørensen gates.

On the theoretical side, the major error sources were studied both mathematically and computationally. This allowed the inspection of the experimental requirements of such gates, thus directing the practical work.

The experimental part consisted mainly in applying a few modifications to the existing apparatus in order to match the needs made clear by the theoretical one. One of them turned out to be more challenging than expected, and is therefore described in a dedicated chapter.

Contents

Chapter 1

Introduction

As the coherent control of very small systems was made possible by the technological improvements made over the second half of last century (among which was the invention of lasers), the idea of exploiting the laws of quantum mechanics in order to build computers with some fundamental advantages over classical machines gained the interest of the scientific community. In particular, intensive research has been motivated by the development of algorithms that drastically reduce the scaling of the runtime on the problem size w.r.t. their classical counterparts, such as the factorisation of large numbers [1], and by the possibility of simulating quantum systems in a more analogous manner, which could for example result into a huge enhancement in the optimisation of chemical processes.

Since the requirements set by the theoretical model of a quantum computer [2] can in principle be fulfilled by various physical systems (among which are superconducting qubits, quantum dots, defects in crystals, and NMR systems), the last decades have seen a technological competition between several candidates aiming to implement such a device. Trapped ions have proven to be one of the most promising among them, as they constitute naturally identical and well characterised quantum bits (qubits) with particularly favourable properties: long coherence times, the possibility to reliably address them by means of lasers for initialisation, manipulation and readout, weak interactions with the environment, controllable qubit-qubit coupling, and the ability to spatially locate them and move them over short distances [3, 4].

In order for a quantum computer to be practically useful, it must be able to work on a large number of qubits, corresponding to the regime where the better scaling of runtime on problem size of quantum algorithms for certain tasks would allow it to outperform a classical machine [5]. This point is normally referred to as *scalability*, and represents one of the main challenges on the path to realising a working QIP system. Indeed, not only is the apparatus required to control several ions currently cumbersome and hard to scale up logistically (as it requires packing more and more optics and electronics around a single device), but also the difficulties in maintaining the coherent control of an ensemble of qubits increase strongly with the size of the system due to technical reasons, such as the increased precision requirements.

This thesis is centred on one of the proposals for improving the logistic scalability of the trapped-ion devices: transport gates. As I will explain in Chap. 5, these reduce the required complexity of both the optical apparatus and the control system. One-qubit transport operations have been demonstrated over the last decade [6, 7], thus it would now be interesting to produce entangling gates working according to this principle, which is exactly what is discussed in this text.

Our aim was to perform the experiment in an existing apparatus based on a linear segmented Paul trap (that will be discussed in Chap. 2). In order to make this possible, a few technical adaptations were needed; in particular, we had to install a new beam path and stabilise a the amplitude of a radio-frequency signal used to trap the ions. The latter modification turned out to be more challenging than expected, thus I will discuss it in a dedicated chapter (Chap. 6).

Chapter 2

The Paul Trap

In principle, atoms in general are very interesting from a QIP perspective, since they are naturally identical and in many of them it is possible to select a set of electronic levels which can be used to define well-behaved qubits: one can find states with long enough decay time to perform quantum computation, and transitions which can be reliably manipulated by means of laser or microwave pulses. Although this is true for both charged and neutral atoms, the disadvantage of the latter comes from the difficulties in providing them with a solid spatial confinement, and from the fact that in most cases their electronic states only show short-range interactions. Ions, on the other hand, can be manipulated by means of electric and magnetic fields, and the Coulomb interaction provides a way of coupling them also when they are several micrometers apart.

There are several schemes for trapping charged particles, the two most commonly used being the Penning and the Paul trap. The first one is based on a strong magnetic field in which the particles orbit – thus being effectively trapped in two directions – while being confined by a static electric field along the direction perpendicular to the orbit plane. The Paul trap is requires only electric fields and allows to keep the particles in a quasi-harmonic potential at a well-defined point in space, making it an ideal choice for laser addressing.

The aim of this chapter is to give a mathematical introduction to the Paul trap, namely to show its equations of motion, their solution, and the approximation we work in. This is of particular interest for this thesis, as much of what was performed in the laboratory was directly connected to the motion of the ions.

2.1 Trapping Potentials

The first temptation when trying to trap a charged particle in vacuum with electric fields is to look for a static-potential configuration with a minimum at the desired point. Unfortunately, Laplace's equation states that it is impossible to create a three-dimensional minimum of the electrostatic potential ϕ at a point with vanishing charge density ρ:

$$\sum_{i=x,y,z} \partial_i^2 \phi(\vec{r}) = \frac{\rho(\vec{r})}{\varepsilon_0} = 0. \tag{2.1}$$

Indeed, to guarantee the validity of this equation at every instant in time, the best one can do is to create an extremum of ϕ ($\partial_i \phi(\vec{r}_0) = 0, \forall i$) confining in two directions (say, $\partial_x^2 \phi(\vec{r}_0), \partial_y^2 \phi(\vec{r}_0) > 0$) at the cost of getting anti-confinement in the third dimension ($\partial_z^2 \phi(\vec{r}_0) < 0$), which corresponds to a so-called *saddle* potential.

Intuitively, it is clear that in such a configuration the particle would "escape" along the anti-confining direction. To prevent this from happening, one might wonder whether it is possible to periodically switch the confining and the anti-confining directions at such a rate that the particle "does not have time to escape" in either of them, while continuously respecting Eq. (2.1) at every point in time. It turns out that this situation (for the case of sinusoidal "switches") can be formally described in terms of the Mathieu equation [8, 9]

$$\frac{\mathrm{d}^2 u}{\mathrm{d}\tau^2} + (a - 2q\,\cos(2\tau))\,u = 0 \tag{2.2}$$

along each direction involved in the switch, and that there are indeed stable solutions to this problem. In general, Eq. (2.2) is solved by functions of the form

$$u(\tau) = Ae^{i\mu\tau} \sum_{r\in\mathbb{Z}} C_{2r} e^{i2r\tau} + Be^{-i\mu\tau} \sum_{r\in\mathbb{Z}} C_{2r} e^{-i2r\tau}, \tag{2.3}$$

where A and B are constants determined by the initial conditions, and C_{2r} and μ are functions of a and q. The stable solutions we are interested in can be interpreted as a slow (compared to the switch rate) harmonic oscillator with some small additional oscillations at the frequency of the switch on top (which are called *micromotion*).

It is possible to choose several different configurations for the electric potentials; the one discussed here (which is also the one employed in our laboratory) consists of a static confinement in one direction together with transverse counter-oscillating potential components (choosing $\vec{r}_0 = \vec{0}$)

$$\phi(\vec{r}, t) = \phi_{\mathrm{dc}}^z\, z^2 + (-\phi_{\mathrm{dc}}^x + \phi_{\mathrm{rf}} \cos(\omega_{\mathrm{rf}} t))\, x^2 + (-\phi_{\mathrm{dc}}^y - \phi_{\mathrm{rf}} \cos(\omega_{\mathrm{rf}} t))\, y^2, \tag{2.4}$$

where $\phi^x_{\rm dc}, \phi^y_{\rm dc}, \phi^z_{\rm dc} > 0$, and $\phi^z_{\rm dc} - \phi^x_{\rm dc} - \phi^y_{\rm dc} = 0$, such that Eq. (2.1) is explicitly fulfilled at any time.

In this section the problem has been presented classically to give the reader an intuitive picture of it. However, the quantum version of the mathematical treatment is conceptually more accurate and not especially more complicated than the classical one, therefore it will be the focus of the next sections.

2.2 Quantum Equations of Motion

The approach presented here was first proposed by Glauber [10] and follows the explanation given in [11]. Since the potential described in Eq. (2.4) does not contain any terms mixing x, y and z, the equations of motion for different spatial directions can be separated. We thus focus on the solution along one of the directions in which the oscillating potential is applied (in the direction with static confinement we obviously have a standard quantum harmonic oscillator). For instance, the Hamiltonian for the motion of the ion in the x direction can be written as

$$\hat{H}_x = \frac{1}{2m}\hat{p}_x^2 + \frac{m}{2}W_x(t)\hat{x}^2, \tag{2.5}$$

where

$$\begin{aligned} W_x(t) &= \frac{\omega_{\rm rf}^2}{4}[a_x + 2q_x\cos(\omega_{\rm rf}t)], \\ a_x &= -\frac{4e\phi^x_{\rm dc}}{m\omega_{\rm rf}^2},\ q_x = \frac{2e\phi^x_{\rm rf}}{m\omega_{\rm rf}^2}, \end{aligned} \tag{2.6}$$

where e is the elementary charge, m is the mass of the ion, $\omega_{\rm rf}$ is the frequency of the oscillating potential, and $\phi^x_{\rm dc}, \phi^x_{\rm rf}$ have been introduced in Eq. (2.4). If we insert Eq. (2.5) into the Heisenberg equations for the operators $\hat{x}$ and $\hat{p}_x$

$$\frac{\mathrm{d}\hat{O}}{\mathrm{d}t} = \frac{1}{i\hbar}[\hat{O}, \hat{H}] \tag{2.7}$$

and combine them, we obtain

$$\frac{\mathrm{d}^2\hat{x}}{\mathrm{d}t^2} + W_x(t)\hat{x} = 0, \tag{2.8}$$

which is Eq. (2.2) with $2\tau = \omega_{\rm rf}t$. It is simple to verify that for two solutions u and v of Eq. (2.8) the expression $u\,\dot{v} - \dot{u}\,v$ is time independent

$$\frac{\mathrm{d}}{\mathrm{d}t}(u\,\dot{v} - \dot{u}\,v) = 0. \tag{2.9}$$

We can now define a special solution u to Eq. (2.8) by the initial conditions

$$u(t=0)=1,\ \dot{u}(t=0)=i\omega_x, \tag{2.10}$$

where $\omega_x = \mu_x\omega_{\text{rf}}/$. This corresponds to imposing $A=1$, $B=0$, $C_{2r}=C_{-2r}$, and $\sum_{r\in\mathbb{Z}} C_{2r}=1$ in Eq. (2.3), i.e.

$$u(t) = e^{i\mu_x\omega_{\text{rf}}t/2}\sum_{s\in\mathbb{N}} 2C_{2s}\cos(s\omega_{\text{rf}}t) = e^{i\mu_x\omega_{\text{rf}}t/2}\Phi(t), \tag{2.11}$$

where $\Phi(t)=\sum_{s\in\mathbb{N}} 2C_{2s}\cos(s\omega_{\text{rf}}t)$ is by definition periodic with periodicity $T_{\text{rf}}=2\pi/\omega_{\text{rf}}$. Given that the operator $\hat{x}(t)$ must be a solution of Eq. (2.8), $u(t)$ can be used to define the time-independent operator (where the time independence follows from Eq. (2.9))

$$\hat{C}(t) = i\sqrt{\frac{m}{2\hbar\omega_x}}[u(t)\dot{\hat{x}}(t)-\dot{u}(t)\hat{x}(t)] \tag{2.12}$$

$$= \hat{C}(0) \tag{2.13}$$

$$= \frac{1}{\sqrt{2m\hbar\omega_x}}[m\omega_x\hat{x}(0)+i\hat{p}(0)], \tag{2.14}$$

which is equal to the annihilation operator $\hat{a}$ of a standard harmonic oscillator with mass m and frequency ω_x

$$\hat{C}(t)=\hat{C}(0)=\hat{a}, \tag{2.15}$$

implying the commutation relation

$$[\hat{C},\hat{C}^\dagger]=[\hat{a},\hat{a}^\dagger]=1. \tag{2.16}$$

The harmonic oscillator associated with $\hat{a}$ is usually called the *reference oscillator* and defines what is classically referred to as *secular motion*. The operators $\hat{x}$ and $\hat{p}_x$ can be re-written in terms of the reference oscillator ladder operators $\hat{a},\hat{a}^\dagger$ and of $u(t)$

$$\hat{x}(t) = \sqrt{\frac{\hbar}{2m\omega_x}}[u^*(t)\,\hat{a}+u(t)\,\hat{a}^\dagger], \tag{2.17}$$

$$\hat{p}_x(t) = \sqrt{\frac{\hbar m}{2\omega_x}}[\dot{u}^*(t)\,\hat{a}+\dot{u}(t)\,\hat{a}^\dagger], \tag{2.18}$$

where we used Eq. (2.9) together with the fact that $u^*(t)$ is also a solution of Eq. (2.8). This form allows us to to draw a useful analogy between our problem and the standard harmonic oscillator, since they share the same algebraic properties. Indeed, we can define a basis of quasi-Fock states

$$\hat{C}(t)\,|0\rangle = \hat{a}\,|0\rangle = 0, \tag{2.19}$$

$$|n\rangle = \frac{(\hat{C}^\dagger(t))^n}{\sqrt{n!}}\,|0\rangle = \frac{(\hat{a}^\dagger)^n}{\sqrt{n!}}\,|0\rangle\,, \tag{2.20}$$

$$\hat{C}(t)\,|n\rangle = \hat{a}\,|n\rangle = \sqrt{n}\,|n-1\rangle\,, \tag{2.21}$$

$$\hat{C}^\dagger(t)\,|n\rangle = \hat{a}^\dagger\,|n\rangle = \sqrt{n+1}\,|n+1\rangle\,. \tag{2.22}$$

These are eigenstates of the number operator

$$\hat{N} = \hat{C}^\dagger(t)\hat{C}(t) = \hat{a}^\dagger\hat{a}, \tag{2.23}$$

but they are not eigenstates of the Hamiltonian, i.e. they cannot be interpreted as energy eigenstates. The intuitive explanation for this is that the time-dependent potential periodically exchanges energy with the motion of the ion, giving rise to the micromotion. Nevertheless, since the micromotion is periodic, fast, and small compared to the reference oscillator, the averages of the energies over one period of modulation T_{rf} are normally used as approximated values for the energy levels of the quasi-Fock states.

It is now interesting to get an expression for the spatial wave functions of the Fock states

$$\psi_n(x,t) = \langle x|n(t)\rangle_S\,, \tag{2.24}$$

where the subscript S indicates the expressions given in the Schrödinger picture. This can be obtained by manipulating Eq. (2.19) and inserting $\hat{p}_x \equiv \partial_x$ into it

$$\begin{aligned}
0 &= \langle x|_S\,\hat{U}(t)\hat{C}(t)\,|0\rangle & (2.25)\\
&= \langle x|_S\,\hat{U}(t)\hat{C}(t)\hat{U}^\dagger(t)\hat{U}(t)\,|0\rangle & (2.26)\\
&= \langle x|_S\,\hat{C}_S(t)\,|0\rangle_S & (2.27)\\
&= \frac{1}{\sqrt{2m\hbar\omega_x}}\,\langle x|_S\,(m\omega_x\dot{u}(t)\hat{x}_S + iu(t)\hat{p}_{x,S})\,|0\rangle_S & (2.28)\\
&= \frac{1}{\sqrt{2m\hbar\omega_x}}(m\omega_x\dot{u}(t)x + iu(t)\partial_x)\,\langle x|0\rangle_S & (2.29)\\
&= \frac{1}{\sqrt{2m\hbar\omega_x}}(m\omega_x\dot{u}(t)x + iu(t)\partial_x)\psi_0(x,t), & (2.30)
\end{aligned}$$

where $\hat{U}(t)$ is the time-evolution unitary operator. Solving the resulting differential equation one gets

$$\psi_0(x,t) = e^{-i\frac{\omega_x}{2}t}\left(\frac{m\omega_x}{\pi\hbar}\right)^{\frac{1}{4}}\frac{1}{\sqrt{\Phi(t)}}e^{-\frac{m\omega_x}{2\hbar}\left(1-i\frac{\dot{\Phi}(t)}{\omega_x\Phi(t)}\right)x^2}, \tag{2.31}$$

and by applying Eq. (2.20) one gets in an analogous manner

$$\psi_n(x,t) = \frac{e^{-i\left(n+\frac{1}{2}\right)\omega_x t}}{\sqrt{2^n n!}} \left(\frac{m\omega_x}{\pi\hbar}\right)^{\frac{1}{4}} \frac{e^{-in\arg(\Phi(t))}}{\sqrt{\Phi(t)}} H_n\left(\sqrt{\frac{m\omega_x}{\hbar|\Phi(t)|^2}}x\right) e^{-\frac{m\omega_x}{2\hbar}\left(1-i\frac{\dot{\Phi}(t)}{\omega_x\Phi(t)}\right)x^2}, \tag{2.32}$$

where H_n is the n-th Hermite polynomial. This is very similar to the wave function of the standard harmonic oscillator, with the addition of periodic modulations due to $u(t)$.

2.3 Lowest-Order Approximation

In order to gain some intuition about the system described in Eq. (2.32) we need to approximate it to the lowest order in the limit where $|a_x|, q_x^2 \ll 1$, and $C_{2r} = 0$, $\forall r > 1$. In this case we can approximate Eq. (2.11) and use Eq. (2.8) to obtain (see Sec. 2.1.1 from [9] for more mathematical details)

$$\mu_x \approx \sqrt{a_x + \frac{q_x^2}{2}} \ll 1, \tag{2.33}$$

$$\omega_x = \frac{\mu_x \omega_{\mathrm{rf}}}{2} \ll \omega_{\mathrm{rf}}, \tag{2.34}$$

$$u(t) \approx e^{i\omega_x t} \frac{1 + \frac{q_x}{2}\cos(\omega_{\mathrm{rf}} t)}{1 + \frac{q_x}{2}}. \tag{2.35}$$

This leads to a normal harmonic-oscillator wave function with the addition of small periodic modulations at the rf frequency, namely the micromotion. To investigate the differences this makes with respect to the reference oscillator, we can substitute Eq. (2.35) into Eq. (2.31), obtaining

$$\psi_0(x,t) \approx e^{-i\frac{\omega_x}{2}t} \left(\frac{m\omega_x}{\pi\hbar}\right)^{\frac{1}{4}} e^{-\frac{m\omega_x}{2\hbar}x^2} \sqrt{\frac{1 + \frac{q_x}{2}}{1 + \frac{q_x}{2}\cos(\omega_{\mathrm{rf}} t)}}\, e^{i\frac{q_x}{2}\frac{m\omega_{\mathrm{rf}}}{2\hbar}\frac{\sin(\omega_{\mathrm{rf}} t)}{1+\frac{q_x}{2}\cos(\omega_{\mathrm{rf}} t)}x^2}, \tag{2.36}$$

which is the standard ground-state wave function of the reference oscillator with a phase and amplitude modulation at frequency $\omega_{\mathrm{rf}}/(2\pi)$. This shows that the micromotion can be treated as a coherent (quasi-classical) oscillation on top of the secular motion. It is also worth noting that the micromotive phase modulation is proportional to x^2, consistent with its minimisation at the node of the potential oscillation.

A tangible example of the coherent behaviour of the micromotion is the following: in the experiments with beryllium[1] ions we need to compensate

[1] The apparatus this thesis was performed on can carry out experiments on both beryllium and calcium ions [12, 13].

for the Doppler shift caused by the axial micromotion in order to maximise the coupling of the laser to the ions. This can be done by modulating the laser frequency with an EOM (electro-optical modulator) driven by a signal which is extracted directly from the one that drives the trap electrodes and is thus in phase with the micromotion itself.

2.4 The Pseudo-Potential Picture

The quantum treatment is the most accurate approach to Paul traps, but also the least mentioned in the literature due to its less intuitive nature. There are two main treatments dominating the literature, both working with classical mechanics: the first one uses the Mathieu equation and is very similar to what is explained above. The second one – which is less rigorous, but works fairly well and is much more intuitive – assumes that the micromotion can be separated from the secular motion and uses the kinetic energy associated to the micromotion as an effective secular potential. Given the spatial distribution of the rf potential, this results into a harmonic pseudo-potential which is consistent to the outcome of the preciser treatment. One can also check a posteriori that the separation between the micromotion and the secular motion is justified.

Together with the “switches” picture that I pointed out in Sec. 2.1, the pseudo-potential provides some intuition about Paul traps, which is going to be helpful while reading the rest of this thesis.

2.5 The Shared Modes of Motion

As mentioned at the beginning of this chapter, the potential configuration used in our experimental apparatus is given by Eq. (2.4). For experimental reasons, it is favourable to use the so-called *linear Paul trap* scheme, where the strength of the confinement is much weaker along one direction than along the other two, giving rise to the formation of a linear chain of ions along that special axis when two or more ions are trapped. In our case this special direction was chosen to be the one along which we apply the static potential, which is called by convention *trap axis* and along which the z axis of our frame of reference is defined.

For the purpose of this thesis we are interested in the behaviour of two ions of the same species in the same potential well. Since the micromotion does not influence the properties of the corresponding reference oscillators, but only adds a small modulation on top of them, it is sufficient to restrict our discussion to the zero-th order approximation of a three-dimensional harmonic potential. Let us consider the motional Hamiltonian for two identical ions (indexed 1 and 2) in the same three-dimensional potential well including the kinetic, harmonic, and Coulomb terms

$$\hat{H} = \frac{\hat{\vec{p}}_1^2}{2m} + \frac{\hat{\vec{p}}_2^2}{2m} + V(\hat{\vec{r}}_1, \hat{\vec{r}}_2), \tag{2.37}$$

where

$$\begin{aligned} V(\hat{\vec{r}}_1, \hat{\vec{r}}_2) &= V_H(\hat{\vec{r}}_1) + V_H(\hat{\vec{r}}_2) + V_C(\hat{\vec{x}}_1, \hat{\vec{x}}_2) && (2.38) \\ &= \frac{m}{2} \sum_{i \in \{x,y,z\}} k_i \hat{r}_{1,i}^2 + \frac{m}{2} \sum_{i \in \{x,y,z\}} k_i \hat{r}_{2,i}^2 + \frac{e^2}{4\pi\varepsilon_0} \frac{1}{|\hat{\vec{r}}_1 - \hat{\vec{r}}_2|}. && (2.39) \end{aligned}$$

The classical equilibrium position of the ions is on the trap axis – due to the weaker axial confinement – and symmetric around the trap centre

$$\vec{r}_{1,2}^{\,equil.} = (0, 0, \pm z_0)^T, \tag{2.40}$$

where z_0 is given by the classical balance between the harmonic force $\vec{F}_H = \vec{\nabla} V_H$ and the Coulomb repulsion $\vec{F}_C = \vec{\nabla} V_C$:

$$z_0 = \left(\frac{e^2}{16\pi\varepsilon_0 k_z} \right)^{\frac{1}{3}} = \left(\frac{e^2}{16\pi\varepsilon_0 \omega_z^2 m} \right)^{\frac{1}{3}}. \tag{2.41}$$

Quantitatively, z_0 is on the order of a few microns and the typical size of the trap electrodes is a few hundred microns, whereas the width of the ground-state wave function $2\hbar/(m\omega_{x,y,z})$ is on the order of nanometres in all spatial directions. This difference in order of magnitude justifies approximating this situation as two coupled harmonic oscillators at the classical equilibrium positions. In this approximation, the potential does not contain any terms mixing x, y and z anymore, thus the motion in different directions can be treated separately. In the following we make the distinction between the axial and the radial directions, and calculate the frequencies of the normal modes of motion.

2.5.1 The Axial Modes

Since we are treating coupled harmonic oscillators with equal masses, the total motional Hamiltonian is diagonalised by the usual normal modes of motion: the centre-of-mass (com) and the stretch mode (str), which can be parametrised respectively as

$$\vec{r}^{\,(1,2)}_{z,\mathrm{com}}(t) = (0, 0, \pm z_0 + z(t))^T, \tag{2.42}$$

$$\vec{r}^{\,(1,2)}_{z,\mathrm{str}}(t) = (0, 0, \pm[z_0 + z(t)])^T, \tag{2.43}$$

where the bracketed superscripts indicate index of the involved ion and multiple superscripts notate a case discrimination. Their frequencies can be found from their wave numbers $k_z = \partial_z^2 V$, which we obtain by inserting Eq. (2.42) and Eq. (2.43), respectively, into the potential given in Eq. (2.39) and differentiating twice with respect to z

$$\omega_{z,\mathrm{com}} = \sqrt{\frac{k_{z,\mathrm{com}}}{m}} = \sqrt{\frac{1}{m}\partial_z^2 V(\vec{r}^{\,(1)}_{z,\mathrm{com}}(t), \vec{r}^{\,(2)}_{z,\mathrm{com}}(t))} = \omega_z, \tag{2.44}$$

$$\omega_{z,\mathrm{str}} = \sqrt{\frac{k_{z,\mathrm{str}}}{m}} = \sqrt{\frac{1}{m}\partial_z^2 V(\vec{r}^{\,(1)}_{z,\mathrm{str}}(t), \vec{r}^{\,(2)}_{z,\mathrm{str}}(t))} = \sqrt{3}\,\omega_z. \tag{2.45}$$

2.5.2 The Radial Modes

As before, the discussion is restricted to the x mode to prevent repetition. Analogously to the case of the axial mode, the Hamiltonian of the shared motion is diagonalised by the centre-of-mass and the "stretch"[2] mode

$$\vec{r}^{\,(1,2)}_{x,\mathrm{com}}(t) = (0, x(t), \pm z_0)^T, \tag{2.46}$$

$$\vec{r}^{\,(1,2)}_{x,\mathrm{str}}(t) = (0, \pm x(t), \pm z_0)^T. \tag{2.47}$$

The frequencies of the modes result in

$$\omega_{x,\mathrm{com}} = \sqrt{\frac{k_{x,\mathrm{com}}}{m}} = \sqrt{\frac{1}{m}\partial_x^2 V(\vec{r}^{\,(1)}_{x,\mathrm{com}}(t), \vec{r}^{\,(2)}_{x,\mathrm{com}}(t))} = \omega_x, \tag{2.48}$$

$$\omega_{x,\mathrm{str}} = \sqrt{\frac{k_{x,\mathrm{str}}}{m}} = \sqrt{\frac{1}{m}\partial_x^2 V(\vec{r}^{\,(1)}_{x,\mathrm{str}}(t), \vec{r}^{\,(2)}_{x,\mathrm{str}}(t))} = \sqrt{\omega_x^2 - \omega_z^2}. \tag{2.49}$$

It is worth noting that the stretch mode here has lower frequency than the centre-of-mass one, in contrast to the axial modes. This can be interpreted as a consequence of the fact that any displacement from the equilibrium position in the radial direction will decrease the Coulomb potential energy, which is not the case in the axial direction.

[2]Strictly speaking, it is not a stretch mode, as the ion chain does not get "stretched". It is going to be called like this anyway in analogy to the axial mode.

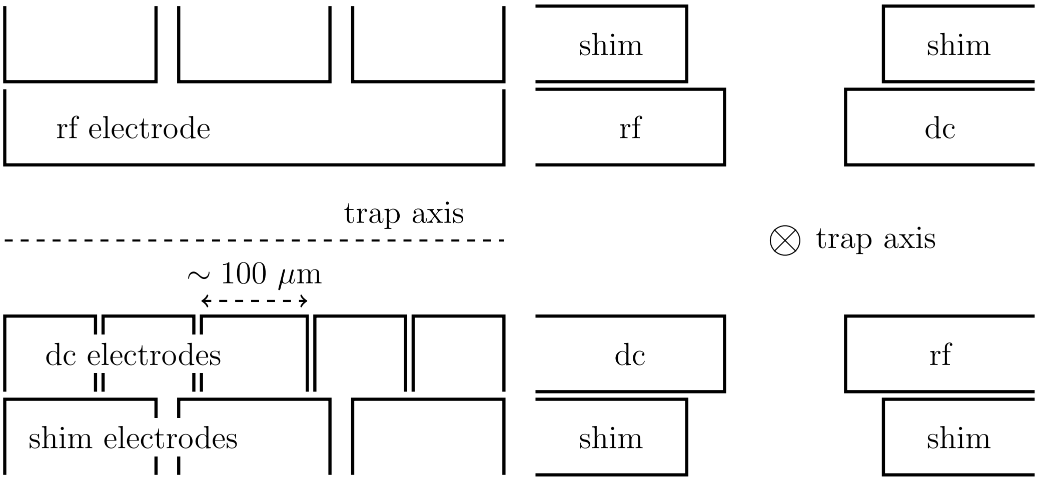

Figure 2.1: Simplified schematics of the segmented Paul trap depicted in two cut views – one coplanar (left) and one perpendicular (right) to the trap axis. The scale and the number of the electrodes are not realistic.

It should also ne noted that for our experimental parameters the spacing between the two radial normal modes is much smaller than in the axial case

$$\omega_{z,\mathrm{str}} - \omega_{z,\mathrm{com}} \sim 2\pi \times 1.5 \text{ MHz} \tag{2.50}$$

$$\omega_{x,\mathrm{com}} - \omega_{x,\mathrm{str}} \sim 2\pi \times 0.14 \text{ MHz} \tag{2.51}$$

This implies that, when performing experiments involving one of them, we have to mind the off-resonant coupling to the other.

Finally, one might be bothered by the fact that the expression Eq. (2.49) is not defined for $\omega_x < \omega_z$. However, this is not a problem, since we operate the trap in the regime where $\omega_x, \omega_y > \omega_z$.

2.6 The Segmented Trap

This section discusses the specific type of trap used to carry out this thesis work. As mentioned before, it is a linear Paul trap, i.e. a trap with static confinement in one direction, and stronger dynamic transverse potentials, as described by Eq. (2.4), confining the ions in a linear chain along the trap axis.

In addition to this, a segmented architecture for the static component of the field is used, that is a series of small dc electrodes is distributed along the whole length of the trap instead of two larger ones at the ends (see Fig. 2.1).

The possibility of modulating the potentials applied to the single electrodes enables the creation of a rich variety of potential profiles along the z axis, opening up to a wide range of experimental possibilities [13, 14], such as

- transport along the axis,
- multiple potential wells, allowing the trapping of separate ion chains,
- merging and splitting of potential wells – hence of ion chains.

The radial confinement, on the other hand, is supplied by large rf electrodes generating a homogeneous potential along the whole trap length, as illustrated in Fig. 2.1.

Further from the trap axis, there is a series of additional large dc electrodes (called *shim electrodes*), which are used to compensate for static stray fields in the radial direction, thus guaranteeing that the equilibrium position of the ions actually corresponds to a minimum of the rf potential amplitude, in order to minimise the micromotion [13].

This segmented architecture is a promising candidate for scaling up to a large-scale quantum computer, as it can be extended with relative ease – at least from the point of view of electronics – to a trapped-ion chip with great local mobility of the qubits [15].

Chapter 3

Laser-Ion Interaction

In ion-trap quantum computing the electronic state of the ion (which is the degree of freedom normally used to define the qubit) is manipulated using lasers – or microwaves, which are not used in our apparatus. It is therefore important to discuss the laser-ion interaction, and in particular the types of transitions that we use for handling beryllium ions.

Before starting, it is worth clarifying a few points about the notation: when describing a system composed of n subsystems indexed by $i \in \{1, \dots, n\}$, the total Hilbert space $\mathcal{H}_{total}$ is given by the tensor product of the Hilbert spaces $\mathcal{H}_i$ of its subsystems

$$\mathcal{H}_{total} = \mathcal{H}_1 \otimes \dots \otimes \mathcal{H}_n. \tag{3.1}$$

In the same way, an operator acting on one of its subsystems (e.g. $\mathcal{H}_i$) can be written as a tensor product of the form

$$\hat{\mathbb{I}}_1 \otimes \dots \otimes \hat{\mathbb{I}}_{i-1} \otimes \hat{O}_i \otimes \hat{\mathbb{I}}_{i+1} \otimes \dots \otimes \hat{\mathbb{I}}_n, \tag{3.2}$$

where $\hat{\mathbb{I}}_j$ is the identity acting on $\mathcal{H}_j$. In the following we will drop all the tensor products and the identity operators, unless specifically required.

Furthermore, the tensor product of two operators acting on different subsystems will not be explicitly written, thus $\hat{A}_i \otimes \hat{B}_j$ will be written as $\hat{A}_i \hat{B}_j$. This is actually consistent with the notation introduced above, given the algebraic rules for tensor products.

3.1 Approximations

As a first step we are going to introduce the approximations that are going to be used throughout this chapter. It will turn out that trapped ions can be described in a special regime of quantum optics, allowing for several useful simplifications.

3.1.1 Semi-Classical Description of Light

The standard Hamiltonian describing the interaction between a light mode defined by the ladder operators $\hat{a}_l, \hat{a}_l^\dagger$ with frequency ω_l and a two-level system with energy difference ω_{eg} between ground $|g\rangle$ and excited state $|e\rangle$ is given by [16]

$$\hat{H} = \hbar\omega_l \left(\hat{a}_l^\dagger \hat{a}_l + \frac{1}{2}\right) + \hbar\frac{\omega_{eg}}{2}\hat{\sigma}_z + \hbar\frac{g}{2}(\hat{\sigma}_+ \hat{a}_l + \hat{\sigma}_- \hat{a}_l^\dagger), \tag{3.3}$$

where $\hat{\sigma}_z = |e\rangle\langle e| - |g\rangle\langle g|$, $\hat{\sigma}_+ = |e\rangle\langle g| = (\hat{\sigma}_-)^\dagger$, and g is the coupling strength.

The laser light used for ion manipulation can be well modelled as a large coherent state of radiation

$$|\alpha\rangle = \hat{\mathcal{D}}(\alpha)\,|0\rangle\,, \;|\alpha| \gg 1, \tag{3.4}$$

where $\hat{\mathcal{D}}(\alpha)$ is the displacement operator. Driving the light mode connected to $\hat{a}_l$ with a laser corresponds to applying the displacement operator to its ground state with an adequate α. If we apply this to Eq. (3.3) and use the fact, that

$$\hat{\mathcal{D}}(-\alpha)\hat{a}_l\hat{\mathcal{D}}(\alpha) = \hat{a}_l + \alpha, \tag{3.5}$$

we obtain an interaction term of the form

$$\hat{H}_{int} = \hbar\frac{g}{2}(\hat{\sigma}_+ \hat{a}_l + \hat{\sigma}_- \hat{a}_l^\dagger) + \hbar\frac{g}{2}(\alpha\hat{\sigma}_+ + \alpha^*\hat{\sigma}_-), \tag{3.6}$$

where the first term accounts for the photon exchange between the light mode and the two-level system, whereas the second one regards light as a purely classical driving field. Since $\alpha \gg 1$, the classical term dominates the interaction. Intuitively, this corresponds to stating that one-photon differences in a laser field are negligible, which is a reasonable approximation. Therefore, in the following the laser light will be considered as a classical driving field [17], and the interaction Hamiltonian will be re-written in the form

$$\hat{H}_{int} = \hbar\frac{\Omega}{2}(e^{i\varphi}\hat{\sigma}_+ + e^{-i\varphi}\hat{\sigma}_-), \tag{3.7}$$

where $\Omega = g\,|\alpha|$ is the so-called Rabi frequency, and φ is defined as the phase of the driving field [1] $\alpha = |\alpha|e^{i\varphi}$ [18].

[1] Recall the correspondence $E(t) = E_0 e^{i(\omega_l t+\varphi)} \propto |\alpha|e^{i(\omega_l t+\varphi)} = \alpha e^{i\omega_l t}$ between the coherent state dimensionless parameter α and the classical field it is associated with.

3.1.2 The Two-Level Atom

In a first approximation, the natural frequency spectrum of the transition between two electronic states is related by a Fourier transform to the spontaneous decay process associated to that transition

$$P(t) = P_0 e^{-t/\tau_1}, \tag{3.8}$$

$$\tilde{P}(\omega) = \mathcal{F}[P](\omega) \propto \frac{1}{(\omega-\omega_0)^2 + \tau_1^{-2}}, \tag{3.9}$$

where ω_0 and τ_1 are the central frequency and the decay time of the transition, respectively. Eq. (3.9) describes a Lorentzian profile with line width Γ inversely proportional to τ_1

$$\Gamma = \tau_1^{-1}. \tag{3.10}$$

The electronic transition that is manipulated in QIP must have a long enough excited-state lifetime τ_1 to allow for a good coherent behaviour (together with a long enough phase coherence time τ_2), implying that the linewidth of the transition between the qubit states is much smaller than the frequency separation from all other states.

The off-resonant coupling of the lasers to undesired transitions (which would populate states outside of the qubit manifold) is minimised by using laser sources with a narrow enough spectrum and with a careful selection of polarisations – since the coupling strength of light to an atomic transition depends strongly on the light polarisation. We can thus approximate the space spanned by the chosen qubit electronic states of the ion during coherent manipulations as a two-level system.

In the case of beryllium ions the qubit-state manipulation is performed by a two-photon Raman process (see Sec. 3.3). Since both of the laser beams driving it are produced by the same source, the effective linewidth of the laser drive (which depends on the relative phase coherence of the two beams) is on the hertz level, despite the linewidth of the laser source itself being on the order of 1 kHz [12].

3.1.3 The Lamb-Dicke Regime

The interaction Hamiltonian of a system composed of a two-level atom with one harmonic-oscillator degree of freedom being driven by a laser is [11]

$$\hat{H}_{int} = \frac{\hbar\Omega}{2}\left(e^{i(\vec{k}_l\cdot\hat{\vec{x}}-\omega_l t-\varphi)}\hat{\sigma}_+ + H.c.\right), \tag{3.11}$$

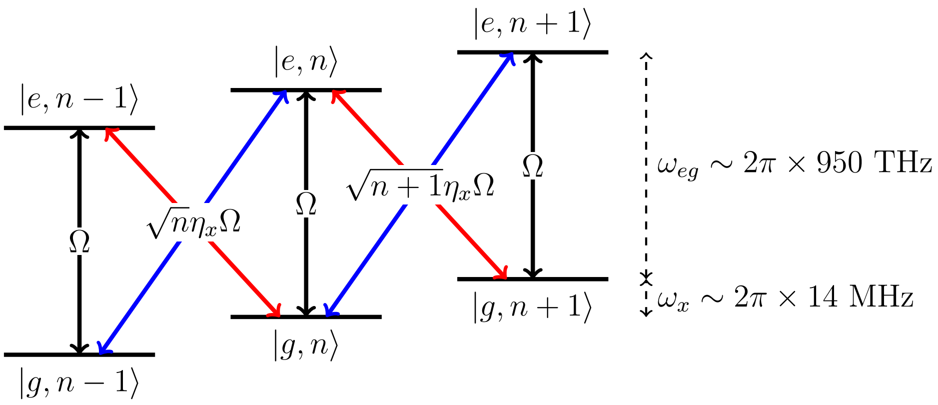

Figure 3.1: The level diagram of the tensor-product space of a qubit and one harmonic oscillator in the Lamb-Dicke regime, with the carrier and first-order sidebands, and their coupling strengths.

where we can rewrite the scalar product in the exponential as

$$\vec{k}_l \cdot \hat{\vec{x}} = \frac{2\pi}{\lambda}\sqrt{\frac{\hbar}{2m\omega_x}}\cos\theta_x(\hat{a}_x + \hat{a}_x^\dagger) \tag{3.12}$$

$$= \eta_x(\hat{a}_x + \hat{a}_x^\dagger). \tag{3.13}$$

We have introduced the so-called Lamb-Dicke parameter η_x, where θ_x is the angle between the wavevector of the laser and the direction of the motional mode. In our apparatus – depending on the geometry of the laser configuration – the Lamb-Dicke parameters for the motional modes of beryllium can reach $\eta_z \sim 0.4$ and $\eta_{x,y} \sim 0.15$. Given that this thesis aims to work with the radial modes, it can be assumed that

$$\eta_x \ll 1, \tag{3.14}$$

thus we can expand the exponential in the Hamiltonian as

$$\begin{aligned} \hat{H}_{int} &= \frac{\hbar\Omega}{2}\left(e^{i(-\omega_l t-\varphi)}\hat{\sigma}_+ + H.c.\right) \qquad (3.15)\\ &+ i\frac{\hbar\eta_x\Omega}{2}\left(e^{i(-\omega_l t-\varphi)}\hat{a}\hat{\sigma}_+ - H.c.\right)\\ &+ i\frac{\hbar\eta_x\Omega}{2}\left(e^{i(-\omega_l t-\varphi)}\hat{a}^\dagger\hat{\sigma}_+ - H.c.\right)\\ &+ \mathcal{O}(\eta_x^2)\\ &= \hat{H}_{carr} + \hat{H}_{RSB} + \hat{H}_{BSB} + \mathcal{O}(\eta_x^2), \qquad (3.16) \end{aligned}$$

where the first term (*carrier*) drives the usual Rabi flops between the qubit states, and the following ones (*red* and *blue sideband*, respectively) additionally imply the exchange of one quantum of motion. These can be understood as different transitions in the tensor-product space of qubit and motional states, as represented in the level diagram 3.1. As we can see from Eq. (3.15), the coupling strength of the sideband transitions is smaller than the carrier by a factor of η_x, but increases with $\sqrt{n}$ as the motion is excited. Higher order terms can be interpreted as transitions involving the exchange of more quanta of motion, and will be suppressed by increasing orders of η_x, thus they can be completely neglected as long as $n = \langle\psi_{\text{motion}}|\, \hat{a}^\dagger\hat{a}\, |\psi_{\text{motion}}\rangle$ is small compared to η_x^{-2}.

Since the transitions and lasers we work with have much smaller linewidth than ω_x, the system can be assumed to be in so-called *sideband-resolved regime*, where one can select exactly which transition to drive with small effect on the others, as formalised in 3.1.4.

As a last remark, it is worth mentioning that η_x depends strongly on the angle between the motional mode and the wavevector of the laser. This can be used to select to what mode of motion we want to couple the light to more strongly by means of the laser geometry, as we will discuss in more detail in Sec. 3.3.

3.1.4 The Rotating-Wave Approximation

Let us consider again a system composed of a qubit and a harmonic oscillator being driven by a laser, assuming it to be in the sideband-resolved regime and in the first-order Lamb-Dicke approximation, and that $\Omega \ll \omega_x$. The Hamiltonian – in the interaction picture with respect to $\hat{H}_0 = \hat{H}_{qubit} + \hat{H}_{motion}$ – is given by

$$\begin{aligned} \hat{H}_I \simeq \; & \frac{\hbar\Omega}{2}\left(e^{i[(\omega_{eg}-\omega_l)t-\varphi]}\hat{\sigma}_+ + H.c.\right) \\ & + i\frac{\hbar\eta_x\Omega}{2}\left(e^{i[(\omega_{eg}-\omega_x-\omega_l)t-\varphi]}\hat{a}\hat{\sigma}_+ - H.c.\right) \\ & + i\frac{\hbar\eta_x\Omega}{2}\left(e^{i[(\omega_{eg}+\omega_x-\omega_l)t-\varphi]}\hat{a}^\dagger\hat{\sigma}_+ - H.c.\right). \end{aligned} \tag{3.17}$$

It can be seen that the time dependence of the terms depends on the laser frequency, which is an experimental parameter that we can precisely and freely tune. If we set ω_l near resonance with one of the transitions, we obtain one slowly-varying term in the Hamiltonian, whereas the others will oscillate at a frequency on the order of ω_x. In our limit it can be shown that the contribution to the time evolution from those fast-oscillating terms is suppressed by

$$\hat{U}_{\text{off resonant}} \propto \frac{\Omega}{\omega_x} \ll 1, \tag{3.18}$$

thus it is possible to neglect them and focus on the resonant transition. What is presented here is a very specific example, but this approximation can be applied to any system having sufficiently narrow transitions and detunings that are much larger than the coupling strength.

3.1.5 The Micromotion Sidebands

In 3.1.3 we assumed that the motion was given by a standard harmonic oscillator. However, as we have seen in chapter 2, this is only a zeroth-order approximation. To study the effect of the dynamic nature of the Paul trap without excessive complications [11], we insert Eq. (2.17) and Eq. (2.11) into the interaction Hamiltonian (in the interaction picture) for the laser-driven two-level ion, and expand the exponential as done in Sec. 3.1.3

$$\begin{aligned}
\hat{H}_I &= \frac{\hbar\Omega}{2}\left(e^{i(k_l\hat{x}(t)-\omega_l t-\varphi)}\hat{\sigma}_+ + H.c.\right) && (3.19)\\
&= \frac{\hbar\Omega}{2}\left(e^{i[\eta_x(u^*(t)\hat{a}_x+u(t)\hat{a}^\dagger)-\omega_l t-\varphi]}\hat{\sigma}_+ + H.c.\right) && (3.20)\\
&\simeq e^{i[(\omega_{eg}-\omega_l)t-\varphi]}\sum_{n\in\mathbb{N}}\frac{(i\eta_x)^n}{n!}\left(e^{-i\omega_x t}\sum_{r\in\mathbb{Z}}C^*_{2r}e^{-ir\omega_{\text{rf}}t}\,\hat{a} + H.c.\right)^n. && (3.21)
\end{aligned}$$

As in Sec. 3.1.4, the resonant terms of this sum can be selected varying laser tuning, in the rotating-wave approximation. It can be seen from this expression that there are additional resonances spaced by multiples of the rf frequency ω_{rf}, which we are going to call *micromotion sidebands*. In our experiment these are normally far detuned from the drive frequency – since $\omega_x \sim 2\pi \times 14$ MHz and $\omega_{\text{rf}} \sim 2\pi \times 114$ MHz – and can thus be neglected.

3.2 The Beryllium Ion

The aim of this section is to give the reader a brief introduction to the ion species that was selected for the purpose of this thesis. More complete information about this topic can be found in [12, **?**].

In our apparatus we can perform experiments with both beryllium ($^9Be^+$) and calcium ($^{40}Ca^+$) ions. For the experiment at which this thesis aims we decided to use beryllium, mainly because it has longer coherence time than the other species.

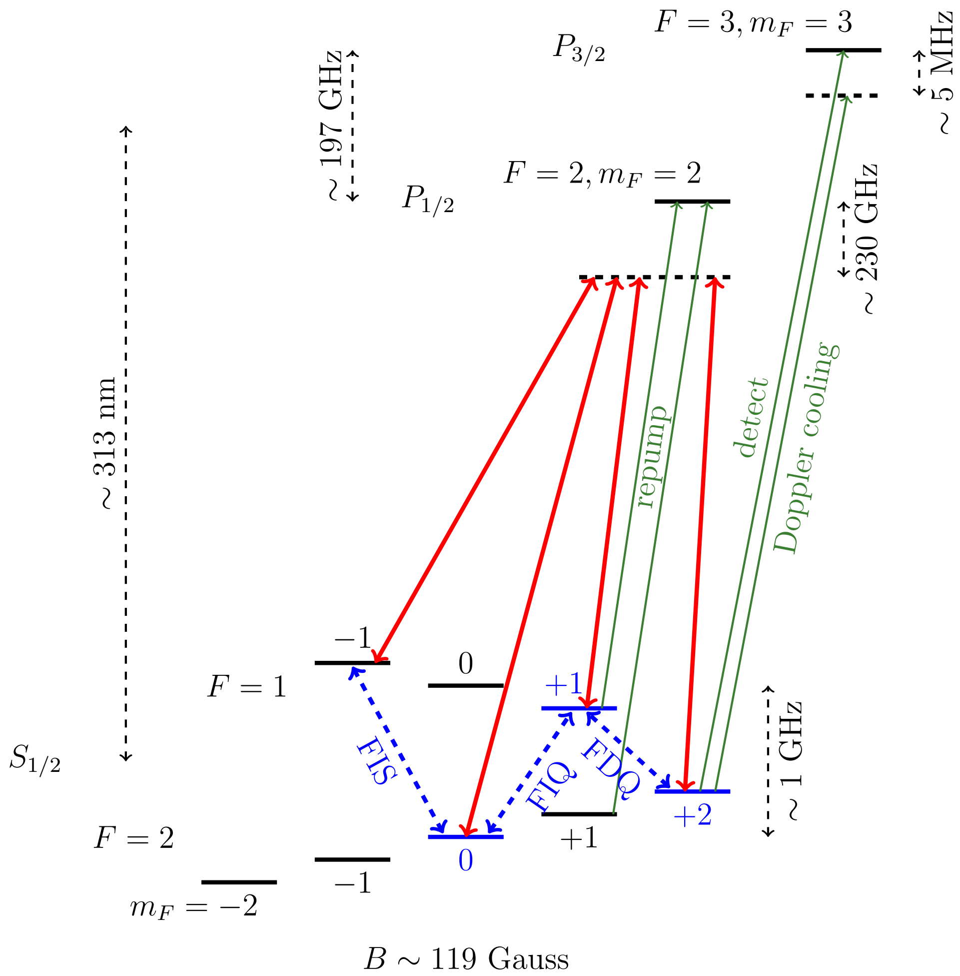

Figure 3.2: Relevant electronic levels and transitions of beryllium ($^9\mathrm{Be}^+$). The red lines represent lasers which are combined to drive the Raman transitions, indicated by the dashed blue lines (FDQ, FIQ, FIS). The green arrows correspond to lasers that excite short-lived states, which decay to $\left|S_{1/2}, F = 2, m_f = 2\right\rangle$ in nanoseconds (for the purpose of detection, cooling, or re-pumping). All lasers have a wavelength of 313 nm, with differences which are very small compared to the total frequency.

At the beginning of every experimental sequence the ion is Doppler cooled to average populations of the motional modes given by $\langle \hat{n}_z \rangle \sim 2$ and $\langle \hat{n}_{x,y} \rangle \sim 0.4$, and its electronic state is initialised to $\left|S_{1/2}, F=2, m_F=2\right\rangle$ by optically pumping. It is also possible to perform sideband cooling – which reduces $\langle n \rangle$ to approximately 0.03 – but this is only done when the requirements on the ion temperature are particularly stringent, as it requires carefully calibrating several experimental parameters (among which are the motional frequencies) and increases the duration of each experiment.

As sketched in figure 3.2, the qubit is encoded in two states of the hyperfine split ground state. In fact, there are two pairs of states that can be used to this end. The first one is called the field-dependent qubit (FDQ) and it is the most straight-forward choice, as it involves the state to which the ion is initialised. Unfortunately, its frequency varies strongly with magnetic-field fluctuations and therefore it has a limited coherence time ($\tau_2 \sim 0.5$ ms). The second possibility is the so-called field-independent qubit (FIQ) and, as the name suggests, it preserves its frequency under small magnetic-field fluctuations, allowing it to stay phase-coherent for $\tau_2 \sim 3.8$ s. This is due to the fact that the two states involved in the transition show Zeeman shifts with equal sign and magnitude around $B \sim 119$ Gauss. The main drawback of the FIQ is that it needs a resonant π pulse on the FDQ both during initialisation and before detection, therefore its contrast depends strongly on the calibration of the FDQ.

The detection of the beryllium internal state is carried out using standard state-selective fluorescence, i.e. the ion is illuminated with a laser resonant with a dipole-allowed transition involving only the state $\left|S_{1/2}, 2, 2\right\rangle$, in the $S_{1/2}$ manifold. This repeatedly drives a fast absorption-and-emission process exclusively if the qubit is in that state. Thus, fluorescence is observed depending on the internal state of the ion, effectively measuring the qubit. The same laser with an additional red detuning is used for the initial Doppler cooling and – together with the repump laser – for initialising the FDQ *bright state* $\left|S_{1/2}, 2, 2\right\rangle$.

The initialisation and detection of the FIQ require several additional steps, since it cannot be directly initialised nor measured like the FDQ. An experimental sequence includes the initialisation via a FDQ π pulse, the qubit manipulation, an additional FDQ π pulse, and detection. The second FDQ π pulse has the effect of transferring the population from the state $\left|S_{1/2}, 1, 1\right\rangle$ to the bright state, effectively enabling the detection of the FIQ state by indirect selective fluorescence.

Since the state $\left|P_{3/2}, 3, 3\right\rangle$ is tens of MHz broad, the detection beam off-resonantly excites a small fraction of the population of the FIQ dark state $\left|S_{1/2}, 2, 0\right\rangle$ (which is only $2\pi \times 200$ MHz away from the bright state) leading to so-called *dark counts*, therefore before applying the final FDQ π pulse and detecting we usually drive a π pulse on the FIS transition to *shelve* the FIQ dark state into $\left|S_{1/2}, 1, -1\right\rangle$, which is further detuned from the bright state.

In our apparatus the hyperfine qubit transitions are manipulated using Raman transitions – which will be explained in Sec. 3.3. Due to this, all lasers we use for beryllium except the ionising one have wavelength around 313 nm, which is generated starting from laser sources in the infrared range (with wavelengths 1050 nm and 1551 nm), which are frequency mixed to obtain 626 nm light, that is finally frequency doubled. With all transitions almost at the same wavelength, the optical setup is shared by all the beams before the individual frequencies are generated in in several separate cavities – e.g. the Raman and the repump lasers use the same infrared sources and initial stage of frequency mixing. The individual timing and frequency fine tunings are controlled using acousto-optical modulators (AOMs).

3.3 The Raman Transitions

As anticipated in Sec. 3.2, the hyperfine-split levels of the beryllium ground state can be coherently coupled to each other via the following mechanism: two states $|g\rangle$ and $|e\rangle$ are coupled to a third level $|f\rangle$ via dipole-allowed transitions, both with an equal detuning (in the case of resonant drive) on the order of $2\pi \times 230$ GHz, as sketched in Fig. 3.3 and Fig. 3.2. This results in driving the transition between $|g\rangle$ and $|e\rangle$ in a two-photon process without populating the third level. Although this looks like an additional technical difficulty – due to the use of two distinct laser frequencies – the hyperfine-split levels are close enough for a single laser modulated by only two different double-pass AOMs to be sufficient.

In the following a short mathematical treatment of Raman transitions is given, which proceeds differently from the derivations that I could find in the literature, but yields equivalent results. For simplicity the motion will be excluded from our treatment. As the central derivation is done, it will be straightforward to recover it in analogy to the standard dipole and quadrupole transitions.

Let us consider a so-called Λ system (see Fig. 3.3), i.e. a level structure consisting of two states $|g\rangle, |e\rangle$ both laser-coupled to a third higher-energetic level $|f\rangle$ with coupling strengths Ω_g, Ω_e (given by the respective laser intensities and dipole matrix elements, e.g. $\Omega_g \propto I_g \langle f| \hat{d} |g\rangle$) and equal detuning Δ. Let us assume that $\Omega_g, \Omega_e \ll \Delta$ and $\omega_{eg} \ll \Delta \ll \omega_{fg}, \omega_{fe}$.

The Hamiltonian for this system can be written in the interaction picture

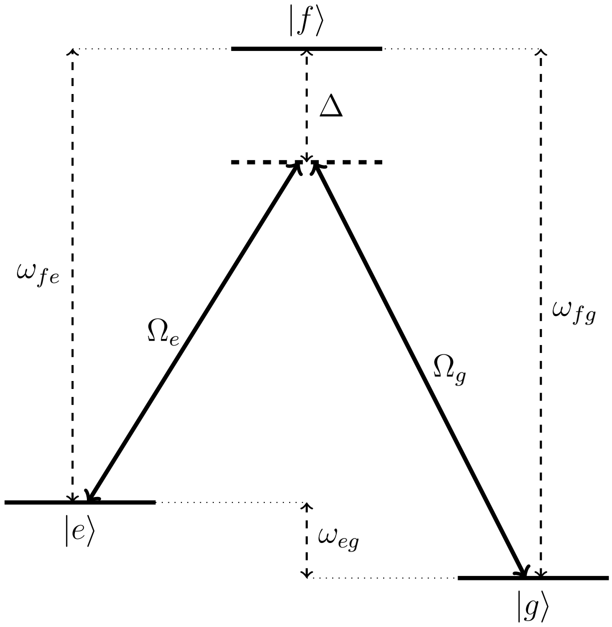

Figure 3.3: Level structure of the states involved in the Raman transition.

as

$$\hat{H}_I = \frac{\hbar\Omega_g}{2}\left(e^{i\Delta t}\,|f\rangle\!\langle g| + H.c.\right) + \frac{\hbar\Omega_e}{2}\left(e^{i\Delta t}\,|f\rangle\!\langle e| + H.c.\right), \tag{3.22}$$

which leads to a time evolution operator $\hat{U}_I$ (interaction picture) that can be calculated with the Magnus expansion [19]

$$\hat{U}_I(t) = e^{\sum_{n\in\mathbb{N}}\hat{M}_n(t)}, \tag{3.23}$$

where

$$\hat{M}_1(t) = -\frac{i}{\hbar}\int_0^t \mathrm{d}t_1 \hat{H}(t_1), \tag{3.24}$$

$$\hat{M}_2(t) = -\frac{1}{2!\hbar^2}\int_0^t \mathrm{d}t_1 \int_0^{t_1} \mathrm{d}t_2 [\hat{H}(t_1), \hat{H}(t_2)], \tag{3.25}$$

$$\begin{aligned}\hat{M}_3(t) = -\frac{i}{3!\hbar^3}\int_0^t \mathrm{d}t_1 \int_0^{t_1} \mathrm{d}t_2 \int_0^{t_2} \mathrm{d}t_3 ([\hat{H}(t_1), [\hat{H}(t_2), \hat{H}(t_3)]] \\ + [\hat{H}(t_3), [\hat{H}(t_2), \hat{H}(t_1)]]),\end{aligned} \tag{3.26}$$

and so forth. By evaluating these expressions one obtains

$$\hat{M}_1(t) = \frac{1}{2\Delta} e^{i\Delta t} (\Omega_g |f\rangle\langle g| + \Omega_e |f\rangle\langle e|) + H.c., \tag{3.27}$$

$$\begin{aligned} \hat{M}_2(t) = &-\frac{i}{4\Delta}\left(t - \frac{\sin(\Delta t)}{\Delta}\right)\big[\Omega_g^2(|f\rangle\langle f| - |g\rangle\langle g|) \\ &+ \Omega_e^2(|f\rangle\langle f| - |e\rangle\langle e|) + \Omega_g\Omega_e(|g\rangle\langle e| + |e\rangle\langle g|)\big], \end{aligned} \tag{3.28}$$

$$\begin{aligned} &\simeq -\frac{i}{4\Delta} t\big[\Omega_g^2(|f\rangle\langle f| - |g\rangle\langle g|) + \Omega_e^2(|f\rangle\langle f| - |e\rangle\langle e|) \\ &\qquad + \Omega_g\Omega_e(|g\rangle\langle e| + |e\rangle\langle g|)\big], \end{aligned} \tag{3.29}$$

$$\hat{M}_n = 0,\ \forall\, n > 2. \tag{3.30}$$

Since $\Omega_g, \Omega_e \ll \Delta$, the term $\hat{M}_1$ only represents a very fast oscillation with minuscule amplitude – corresponding to the far-off-resonant excitation of $|f\rangle$ – and can therefore be neglected. This approximation is called *adiabatic elimination* of $|f\rangle$.

Regarding $\hat{M}_2$, its time dependence contains two contributions: one grows linearly with time and the other is a very fast oscillation with small amplitude, which can be neglected analogously to $\hat{M}_1$. The remaining expression Eq. (3.29) can be split into two parts with different effects. The first two terms effectively shift the energy levels of $|g\rangle$, $|e\rangle$, and $|f\rangle$ (this can be easily understood by transforming to Schrödinger picture) as a consequence of the off-resonant couplings, resulting into the so-called *AC Stark shift*

$$\tilde{\omega}_{eg} = \omega_{eg} + \frac{\Omega_g^2 - \Omega_e^2}{4\Delta}. \tag{3.31}$$

The third term drives Rabi flops between $|g\rangle$ and $|e\rangle$ with an effective Rabi frequency

$$\Omega = \frac{\Omega_g \Omega_e}{4\Delta}. \tag{3.32}$$

To summarise, this results in a means to coherently drive the transition between these two states with a two-photon process mediated by an off-resonant state which we can adiabatically eliminate. Note that the approach presented here is based on a simplistic model, which describes the Raman transition adequately, but is insufficient to completely characterise the AC Stark shift. Indeed, since $\omega_{eg} \ll \Delta$, both $|g\rangle$ and $|e\rangle$ are in fact shifted by both lasers, whereas we assumed each laser to couple to only one of the states. Furthermore, in beryllium there are also other levels in the $P_{1/2}$ manifold (to which the state $|f\rangle$ belongs) contributing to the total AC Stark shift [20].

Raman transitions formally behave the same as standard dipole or quadrupole ones, but some additional care must be taken when trying to add a detuning

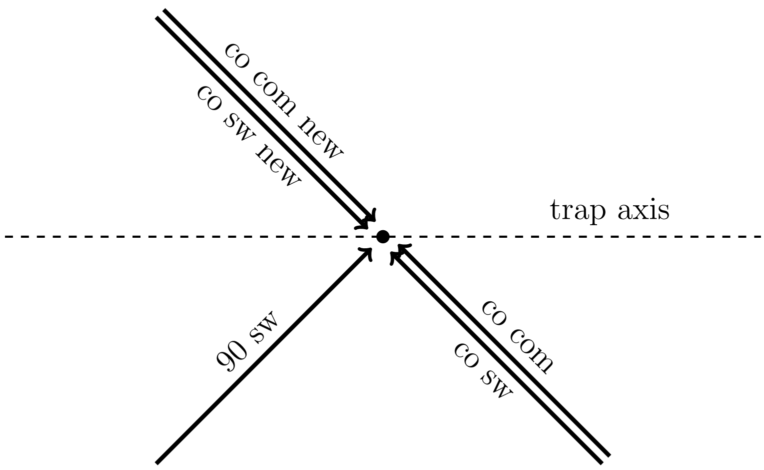

Figure 3.4: Possible laser geometries at our disposal in the laboratory.

to the transition frequency, e.g. in order to drive a motional sideband. Indeed, by looking at the level diagram 3.3, one can see that red-detuning the effectively driven transition requires us to blue-detune the lowest-frequency laser and to leave the other at the same frequency, and vice versa for the blue detuning. This is a consequence of the fact that the frequency of the driven transition is given by the difference between the two drive frequencies (due to energy conservation).

If we were to take coupling to the ion motion into account (which is not done explicitly here), we would find that the effective wavevector associated with the Raman transition is given by the difference between the wavevectors of the two drive lasers

$$\vec{k} = \vec{k}_g - \vec{k}_e, \tag{3.33}$$

consistent with momentum conservation. This can be useful, as it allows one to select which modes of motion the lasers couple to simply by changing the laser geometry (as mentioned in section 3.1.3). Indeed, in the laboratory we can choose among the following configurations (see figure 3.3):

- **co-co:** co com + co sw,
- **co-co new:** co com new + co sw new,
- **co-90:** co com + 90 sw,
- **co-90 new:** co com new + 90 sw.

Given that the frequency of the lasers is on the order of 950 THz and the difference between the two beams is around 1 GHz, it is clear that the first two configurations lead to a negligible coupling to the motion, since $|\vec{k}_{\text{co-co}}| = |\vec{k}_g| - |\vec{k}_e| \ll |\vec{k}_g|, |\vec{k}_e|$, whereas the others imply $|\vec{k}_{\text{co-90}}| = (|\vec{k}_g| + |\vec{k}_e|)/\sqrt{2}$. The difference between the two co-90 configurations is the direction of $\vec{k}$: in co-90 it is nearly perfectly axial, and in co-90 new it is purely radial (both with an angular deviation on the order of $(|\vec{k}_g| - |\vec{k}_e|)/(|\vec{k}_g| + |\vec{k}_e|) \sim 10^{-6}$) thus coupling exclusively to the axial and to the radial modes, respectively. Obviously, the last point is only valid if we assume perfect alignment of the beams to the trap, which is unrealistic. In the laboratory the undesired coupling to the orthogonal modes is dominated by the imperfections in the beam alignment, but its effect is usually suppressed by the fact that they are off-resonant from the one we want to drive.

On the optical table the distribution of light among the beams works as follows [12, 13]: after producing 313 nm light as mentioned in Sec. 3.2, two polarising beam splitters (PBS) distribute it between the co com, co sw, and 90 sw beam paths, where the frequencies and timings of the beams are controlled using AOMs. Finally, the lasers are coupled into the trap using optical fibres and mirrors.

The experiment discussed in this thesis is the first that operates with the radial modes on this setup, therefore we had to add the optics required for the new beams. The most straightforward way was deflecting the light going to the co-co into another fibre going to the other side of the trap, as it allows the use of the existing AOMs and control system without any modifications. In order to be able to switch between the old and the new configurations, the deflection is carried out using a mirror placed on a magnetic mount, which can be inserted and removed by hand.

As a final remark about Raman transitions, it is worth mentioning an effect that results from the treatment of the motion, which does not occur in dipole and quadrupole transitions. Depending on the laser geometry, it is possible to set the frequency difference between the drive lasers to match the frequency of one of the motional modes to which they can couple, therefore driving exclusively the motion without involving the internal state of the ions. This can be used, for example, to realise the so-called *phase gate*, as shown in [6].

3.4 The Final Hamiltonian

The main results of this chapter are summarised by the well-known Hamiltonian for the interaction between a semi-classical laser and a two-level ion trapped in a three-dimensional harmonic potential in the first-order Lamb-

Dicke approximation

$$\begin{aligned}\hat{H}_I \simeq & \frac{\hbar\Omega}{2}\left(e^{i[(\omega_{eg}-\omega_l)t+\varphi]}\hat{\sigma}_+ + H.c.\right) \qquad (3.34)\\ & + \sum_{q=x,y,z} i\frac{\hbar\eta_q\Omega}{2}\left(e^{i[(\omega_{eg}-\omega_q-\omega_l)t+\varphi]}\hat{\sigma}_+\hat{a}_q - H.c.\right)\\ & + \sum_{q=x,y,z} i\frac{\hbar\eta_q\Omega}{2}\left(e^{i[(\omega_{eg}+\omega_q-\omega_l)t+\varphi]}\hat{\sigma}_+\hat{a}_q^\dagger - H.c.\right)\\ & = \hat{H}_{carr} + \sum_{q=x,y,z}\hat{H}_{RSB}^{(q)} + \sum_{q=x,y,z}\hat{H}_{BSB}^{(q)}, \qquad (3.35)\end{aligned}$$

which can potentially be further simplified by applying the rotating-wave approximation as soon as the laser frequency scale is known. Extending this to many ions and lasers is straightforward, and will be the starting point for the mathematical treatment of the entangling gate we aim to carry out – the Mølmer Sørensen gate.

Chapter 4

The Mølmer Sørensen Gate

In the last twenty years the Mølmer Sørensen (MS) gate has become the most popular type of entangling gate in trapped ions, because of its robustness and relative experimental simplicity [21, 22, ?, 23, 24]. First of all, its effect is independent of the motional state of the ions (in the Lamb-Dicke approximation), allowing one to reach high fidelity with imperfect cooling [25, 26, 27]. Also, it does not require single-ion addressing with the lasers, which is challenging on a practical level; the addressing beams are difficult to localise on a single qubit without crosstalk.[1].

In this chapter, I will start with a few general considerations about entangling gates in trapped ions, then briefly summarise the mathematics for the MS gate, and finally discuss the experimental limitations and error sources.

4.1 Entangling Gates in Trapped Ions

In general, an entangling gate on n qubits is a unitary acting on the n-qubit Hilbert space $\hat{U} \in \mathcal{H}_{\text{qubit}}^{\otimes n}$, which is able to map separable states to entangled states and vice versa. From a physical point of view, this is a consequence of some separable states not being eigenstates of the Hamiltonian describing the gate, which implies that the qubit states interact with each other. Therefore, in order to produce such gates one needs to implement a controlled interaction between the physical qubit degrees of freedom.

In trapped ions this is not trivial, as one of the reasons they make good qubits is that their internal state interacts weakly with everything apart from electromagnetic radiation – in contrast to several other QIP implementations (e.g. nuclear magnetic resonance systems), where one of the main efforts

[1]This advantage of not needing single-ion addressing is however lost as soon as such a gate is applied to two ions out of a larger chain.

is rather to minimise the unavoidable interactions. Unfortunately, coherent electromagnetic coupling (via single-photon exchange) is not a mechanism we can exploit in trapped ions, since it is slow compared to laser manipulations, and it would require embedding the ions in a high-finesse cavity, which would imply additional challenges.

However, by examining the final Hamiltonian Eq. (3.34), we see that the entanglement between the internal and motional state of the ion can be engineered by driving the motional sidebands. This is interesting, because the motion of n ions in the same harmonic well is coupled by their Coulomb repulsion (as explained in section 2.5), therefore it can bridge the interaction between the qubits. This approach is efficient and very well controllable, as the interaction between the internal and motional state relies entirely on the laser drive, which we control directly.

Formally, over one gate time we are going to entangle the two-qubit internal state to one of the shared states of motion, let the system evolve, and separate them in such a way that the final state is going to be the tensor product of a two-qubit entangled state and the initial motional state

$$\left|\psi_1^0\right\rangle_1 \otimes \left|\psi_2^0\right\rangle_2 \otimes \left|\psi_m^0\right\rangle_{\text{mot}} \longrightarrow |\psi(t)\rangle_{1,2,\text{mot}}^{\text{ent}} \longrightarrow |\psi_{final}\rangle_{1,2}^{\text{ent}} \otimes \left|\psi_m^0\right\rangle_{\text{mot}}, \quad (4.1)$$

where the superscript *ent* labels entangled states and the subscripts 1, 2, and *mot* indicate the components of the Hilbert space relative to the first and the second qubit state and the motional degree of freedom, respectively.

4.2 State-Dependent Force

Before starting the complete treatment of the MS gate, it is worth considering a simpler example [28], which is useful to obtain some intuition about the central topic of this chapter. Let us consider applying a laser field composed of an equal superposition of the first red and blue motional sidebands to a single ion, assuming both laser contributions to have phase $\varphi = -\pi/2$. From Eq. (3.34) it follows that the Hamiltonian in the interaction picture, after applying the first-order Lamb-Dicke approximation and rotating-wave approximations is given by

$$\hat{H}_I = \frac{\hbar\eta_x\Omega}{2}(\hat{a}_x + \hat{a}_x^\dagger)\hat{\sigma}_x, \quad (4.2)$$

where η_x is the Lamb-Dicke parameter, Ω the Rabi frequency, $\hat{a}$ and $\hat{a}^\dagger$ the ladder operators of the x mode of motion (which we assume to be the only one resonant with the laser), and $\hat{\sigma}_x$ the Pauli x operator acting on the qubit.

This leads to the following unitary evolution

$$\hat{U}_I(t) = \hat{\mathcal{D}}\left(-i\frac{\eta_x \Omega t}{2}\hat{\sigma}_x\right) \tag{4.3}$$

$$= \hat{\mathcal{D}}\left(-i\frac{\eta_x \Omega t}{2}\right)|+\rangle\langle+| + \hat{\mathcal{D}}\left(i\frac{\eta_x \Omega t}{2}\right)|-\rangle\langle-|, \tag{4.4}$$

where $\hat{\mathcal{D}}$ is the coherent displacement operator and $|\pm\rangle = (|0\rangle \pm |1\rangle)/\sqrt{2}$. For an initial state $|0\rangle_{\text{qubit}}|0\rangle_{\text{motion}} = (|+\rangle + |-\rangle)|0\rangle/\sqrt{2}$, this gives rise to the following time evolution

$$|\psi(t)\rangle = \frac{|+\rangle\left|-i\frac{\eta_x \Omega t}{2}\right\rangle + |-\rangle\left|i\frac{\eta_x \Omega t}{2}\right\rangle}{\sqrt{2}}. \tag{4.5}$$

In the motional phase space this corresponds to splitting the ground-state wavepacket into two coherent components (one related to $|+\rangle$ and one to $|-\rangle$) and displacing them in opposite directions, generating a so-called *Schrödinger's cat state* of qubit and motion. This mechanism is exploited, for example, in the creation of grid states [29].

If a symmetric detuning to the laser components (i.e. detuning the blue sideband by $+\delta$ and the red by $-\delta$) was added, it would result in an additional time dependence in the Hamiltonian Eq. (4.2)

$$\hat{H}_I = i\hbar\eta_x\Omega(e^{i\delta t}\hat{a}_x - e^{-i\delta t}\hat{a}_x^\dagger)\hat{\sigma}_x, \tag{4.6}$$

obtaining the time evolution (up to a global phase)

$$\hat{U}_I(t) = \hat{\mathcal{D}}\left(\frac{\eta_x\Omega}{\delta}[e^{-i\delta t} - 1]\right)|+\rangle\langle+| + \hat{\mathcal{D}}\left(\frac{\eta_x\Omega}{\delta}[e^{-i\delta t} - 1]\right)|-\rangle\langle-|, \tag{4.7}$$

which can be interpreted in motional phase space as the same *cat components* as above making circular loops in opposite directions.

4.3 Mathematics of the Mølmer Sørensen Gate

This section derives the time evolution following from the Mølmer Sørensen Hamiltonian, defining the gate based on that result, and shows a simple special case in order to develop some intuition about it.

4.3.1 General Time Evolution

The idea behind the MS gate [25, 27] is similar to the one presented in Sec. 4.2, however with two qubits: we trap two ions in the same potential well and drive them with a laser containing equal contributions of two frequencies, symmetrically detuned by $\pm\delta$ with respect to the first red and blue sidebands (relative to one of the shared modes of motion), with $|\delta| \ll \omega_{\text{motion}}$ and $|\delta| \ll |\omega_{\text{str}} - \omega_{\text{com}}|$. The Hamiltonian for this situation – always in the interaction picture and with the same set of approximations as in Sec. 4.2 – is then

$$\hat{H}_{MS}(t) = \frac{\hbar\eta\Omega(t)}{2}\left(e^{i\delta(t)t}\hat{a} + e^{-i\delta(t)t}\hat{a}^\dagger\right)\hat{S}_{\varphi_1,\varphi_2}, \tag{4.8}$$

$$\hat{S}_{\varphi_1,\varphi_2} = \hat{\sigma}^{(1)}_{\varphi_1} + \hat{\sigma}^{(2)}_{\varphi_2}, \tag{4.9}$$

$$\hat{\sigma}^{(i)}_{\varphi} = e^{i\varphi}\hat{\sigma}^{(i)}_{+} + e^{-i\varphi}\hat{\sigma}^{(i)}_{-}, \tag{4.10}$$

where $\hat{a}, \hat{a}^\dagger, \eta$ are related to the selected shared mode of motion, φ_1 and φ_2 are the respective relative phases of the laser to the qubits (which are labelled as 1 and 2), and the superscript (i) indicates on which qubit the operator $\hat{\sigma}^{(i)}_{\varphi}$ acts. With respect to Eq. (3.34), the phases have been redefined as $\varphi_i \to \varphi_i - \pi/2$ for convenience. Note that the coupling strength and the detuning can be time-dependent.

The time evolution of this system can be calculated with the Magnus expansion (as in Sec. 3.3). The mathematics for evaluating the terms in the expansion is straightforward, and leads to

$$\hat{M}_1 = (\alpha(t)\hat{a}^\dagger - \alpha(t)^*\hat{a})\hat{S}_{\varphi_1,\varphi_2}, \tag{4.11}$$

$$\hat{M}_2 = -i\Phi(t)\hat{S}^2_{\varphi_1,\varphi_2}, \tag{4.12}$$

$$\hat{M}_n = 0,\ \forall n > 2, \tag{4.13}$$

where

$$\alpha(t) = -i\frac{\eta}{2}\int_0^t \mathrm{d}t_1\Omega(t_1)e^{-i\delta(t_1)t_1}, \tag{4.14}$$

$$\Phi(t) = \frac{\eta^2}{4}\int_0^t \mathrm{d}t_1\int_0^{t_1}\mathrm{d}t_2\Omega(t_1)\Omega(t_2)\sin\big(\delta(t_1)t_1 - \delta(t_2)t_2\big) \in \mathbb{R}, \tag{4.15}$$

and therefore

$$\hat{U}_{MS}(t) = \hat{\mathcal{D}}\Big(\alpha(t)\hat{S}_{\varphi_1,\varphi_2}\Big)\, e^{-i\Phi(t)\hat{S}^2_{\varphi_1,\varphi_2}}, \tag{4.16}$$

where we could separate the exponential because $\hat{M}_1$ and $\hat{M}_2$ commute. We obtained two distinct contributions, which can be interpreted as a state-dependent coherent drive of the motion (as in Sec. 4.2) and a state-dependent phase accumulation respectively. It is simple to show that $\Phi(t)$ is proportional to the area in phase space included by the trajectory of $\alpha(t)$ [23]

$$\Phi(t) = -\,\mathrm{Im}\left\{\int_0^t \mathrm{d}\alpha(t')\,\alpha(t')^*\right\}, \tag{4.17}$$

which is normally referred to as a *geometric phase*.

To understand the action of this time evolution on the two-qubit state, we consider the two-qubit eigenstates of the Hamiltonian, which are given by tensor products of the eigenstates of $\hat{\sigma}_\varphi$

$$|\pm_\varphi\rangle = \frac{|0\rangle \pm e^{i\varphi}|1\rangle}{\sqrt{2}} \tag{4.18}$$

$$\hat{\sigma}_\varphi |\pm_\varphi\rangle = \pm |\pm_\varphi\rangle . \tag{4.19}$$

Given that $\hat{S}^2_{\varphi_1,\varphi_2} = 2(\hat{\mathbb{I}} + \hat{\sigma}^{(1)}_{\varphi_1}\hat{\sigma}^{(2)}_{\varphi_2})$, if we apply Eq. (4.16) to a general initial state for the MS gate (i.e. the motion is initially disentangled from the two-qubit state)

$$|\psi_0\rangle = \frac{a_1\left|+^{(1)}_{\varphi_1}+^{(2)}_{\varphi_2}\right\rangle + a_2\left|+^{(1)}_{\varphi_1}-^{(2)}_{\varphi_2}\right\rangle + a_3\left|-^{(1)}_{\varphi_1}+^{(2)}_{\varphi_2}\right\rangle + a_4\left|-^{(1)}_{\varphi_1}-^{(2)}_{\varphi_2}\right\rangle}{2}|\alpha_0\rangle , \tag{4.20}$$

we obtain

$$\begin{aligned} \hat{U}_{MS}(t)|\psi_0\rangle = & \frac{a_1 e^{-i4\Phi(t)}}{2}\left|+^{(1)}_{\varphi_1}+^{(2)}_{\varphi_2}\right\rangle |\alpha_0 + 2\alpha(t)\rangle \\ & + \frac{a_2}{2}\left|+^{(1)}_{\varphi_1}-^{(2)}_{\varphi_2}\right\rangle |\alpha_0\rangle \\ & + \frac{a_3}{2}\left|-^{(1)}_{\varphi_1}+^{(2)}_{\varphi_2}\right\rangle |\alpha_0\rangle \\ & + \frac{a_4 e^{-i4\Phi(t)}}{2}\left|-^{(1)}_{\varphi_1}-^{(2)}_{\varphi_2}\right\rangle |\alpha_0 - 2\alpha(t)\rangle , \end{aligned} \tag{4.21}$$

which describes a trajectory in phase space and the corresponding geometric-phase accumulation conditional on the two-qubit state.

4.3.2 The Gate Time

From Eq. (4.21) it is clear that during most of the time evolution the motional state is entangled with the two-qubit state, which is not desirable for our quantum gate. Therefore, $\delta(t)$ and $\Omega(t)$ should be set so that at some point t_g in time (which is called *gate time*) $\alpha(t)$ vanishes. When this is valid, we can write the effect of Eq. (4.16) as a gate acting on the two-qubit Hilbert space

$$\hat{U}_{MS}(t_g) = \hat{U}_{2\ \mathrm{qubit}} \otimes \hat{\mathbb{I}}_{\mathrm{motion}}. \tag{4.22}$$

As an example, one can calculate the effect this will have on the initial two-qubit state $|\psi_0\rangle = |00\rangle|\alpha_0\rangle$

$$\hat{U}_{MS}(t_g)|\psi_0\rangle = \frac{1}{2}\left[\left(e^{-i4\Phi(t_g)} + 1\right)|00\rangle + e^{i(\varphi_1+\varphi_2)}\left(e^{-i4\Phi(t_g)} - 1\right)|11\rangle\right]|\alpha_0\rangle , \tag{4.23}$$

which is a maximally entangled state of the two qubits for $\Phi(t_g) = \pi/8 + n\pi/4$, $\forall n \in \mathbb{Z}$, and is a separable state of qubits and motion.

This discussion also shows one of the main advantages of the MS gate over alternate techniques: the action of $\hat{U}_{MS}(t_g)$ on the qubits is independent of α_0, which means that the gate can operate on "hot" ions – as long as their state of motion does not cause any of our approximations to break down.

4.3.3 Gate Implementation with a Square Pulse

It is now interesting to evaluate $\alpha(t)$ and $\Phi(t)$ explicitly for the simplest possible case, namely $\delta, \Omega \equiv$ const. This is equivalent to a square pulse, which is a good approximation for the standard pulse shaping we use in beryllium experiments[2] – not at all for transport gates, though, as will be discussed in Chap. 5. Calculating Eq. (4.14) and Eq. (4.15) for this case is straightforward and leads to

$$\alpha(t) = \frac{\eta\Omega}{2\delta}\left(e^{-i\delta t} - 1\right), \tag{4.24}$$

$$\Phi(t) = \frac{\eta^2\Omega^2}{4\delta}\left(t - \frac{\sin(\delta t)}{\delta}\right). \tag{4.25}$$

Given the condition $\alpha(t_g) = 0$, the gate time can be set to $t_g = 2\pi n/\delta$, $\forall\, n \in \mathbb{Z}$, implying

$$\Phi(t_g) = \frac{\eta^2\Omega^2}{4\delta} t_g = \frac{\pi\eta^2\Omega^2}{2\delta^2} n,\ n \in \mathbb{Z}, \tag{4.26}$$

which can also be used to set the experimental parameters based on the desired effective action of the gate.

4.4 Error Sources and Experimental Issues

As shown above, MS gates can significantly reduce the experimental difficulties with respect to many other entangling schemes for trapped ions, most importantly enabling the production of high-fidelity gates with imperfect cooling and without requiring single-ion laser addressing. However, for the physical realisation it is important to investigate the effect of other error sources, in order to direct the focus of our experimental efforts.

[2] In the laboratory we use square pulses for all single-ion gates and beryllium experiments. Since calcium has smaller Lamb-Dicke parameter and motional frequencies than beryllium, multi-qubit gates with calcium and mixed species require some pulse shaping to minimise the effect of the off-resonant coupling to the carrier.

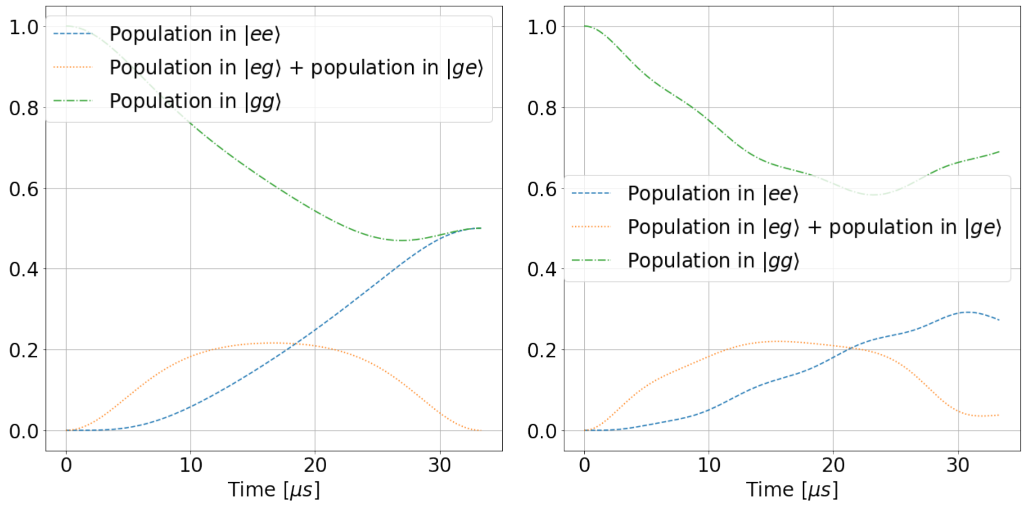

Figure 4.1: Comparison between the simulated time evolution of the two-qubit populations during an ideal square-pulse MS gate (left) and the same with the off-resonant excitation of the stretch mode (right). All the simulations in this thesis have been performed with QuTiP [31].

The effects presented in this section can be analysed in the simple case of the square pulse, as they are not determined directly by the time dependence of Ω and δ. Other experimental issues specific to this time dependence will be discussed in Chap. 5. A more extensive discussion about the effect of various noise sources on entangling gates in trapped ions can be found in [30].

4.4.1 Off-Resonant Couplings

As mentioned before, we usually work in the rotating-wave approximation, which means that we neglect the off-resonant terms. However, some care must be taken when defining the range of validity of such an approximation, because in the experiment at which this thesis aims, not all transitions are sufficiently far detuned. Indeed, a peculiarity of the radial modes of motion is that the frequency difference between the centre-of-mass and the stretch mode is not as large as for the axial modes – as shown in Sec. 2.5.2.

More quantitatively – given that with beryllium in our apparatus the frequencies are typically $\omega_x \sim 2\pi \times 15$ MHz, $\omega_y \sim 2\pi \times 13$ MHz, and $\omega_z \sim 2\pi \times 2$ MHz – when working on the x mode it is valid that the carrier, the axial sidebands, and the y sidebands are far off resonance, but from Eq. (2.47)

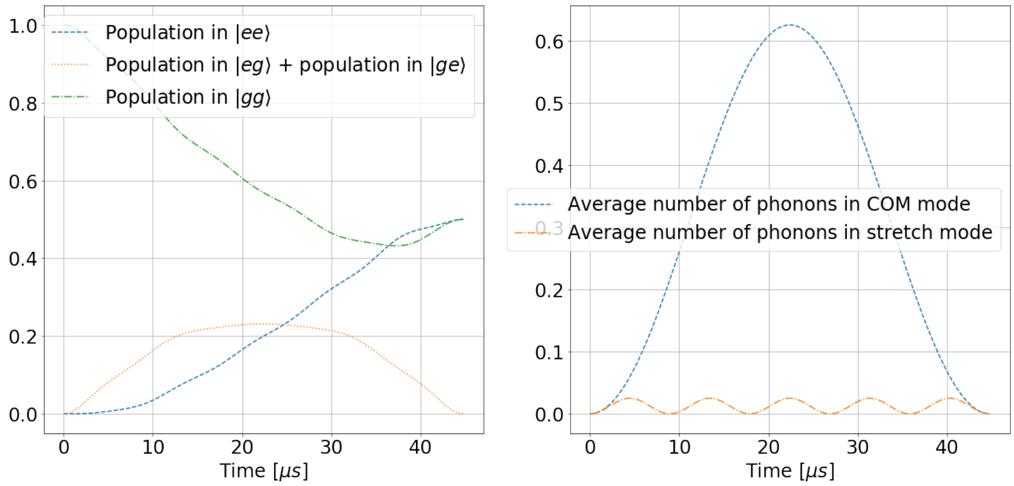

Figure 4.2: Simulated results of the proposed correction for the off-resonant coupling to the stretch mode. The image on the left shows the correct behaviour of the populations at the gate time and the increased sensitivity to timing errors. As can be seen in the image on the right, the motion of both modes gets perfectly disentangled from the qubits at the gate time.

it turns out that $\omega_{x,\mathrm{com}}$ and $\omega_{x,\mathrm{str}}$ are only $\sim 2\pi \times 130$ kHz apart, which is too small for the rotating-wave approximation to hold. Indeed, when comparing the simulations for a square pulse with and without taking into account the off-resonant coupling to the stretch mode (see Fig. 4.1), it is clear that the undesired mode gets populated significantly and that this affects the gate fidelity strongly – it drops from 99.998% to 91%.

Since the modes cannot be shifted, it is necessary to find a workaround to this problem. One possibility is to consider the stretch mode as a "second gate mode", and to try to match the detuning and the laser intensity to drive a gate on that mode simultaneously, or at least to disentangle it from the motion at the gate time. Assuming that the main mode we drive is the centre-of-mass, this situation can be described by the Hamiltonian

$$\hat{H}_{MS}^{tot} = \hat{H}_{MS}^{\mathrm{com}} + \hat{H}_{MS}^{\mathrm{str}} \tag{4.27}$$

$$= \frac{\hbar\eta\Omega}{2}\left[\left(e^{i\delta t}\hat{a}_{\mathrm{com}} + e^{-i\delta t}\hat{a}_{\mathrm{com}}^{\dagger}\right) + \left(e^{i(\delta+\Delta)t}\hat{a}_{\mathrm{str}} + e^{-i(\delta+\Delta)t}\hat{a}_{\mathrm{str}}^{\dagger}\right)\right]\hat{S}_{\varphi_1,\varphi_2} \tag{4.28}$$

where $\Delta = \omega_{x,\mathrm{com}} - \omega_{x,\mathrm{str}}$. Since $[\hat{H}_{MS}^{\mathrm{com}}, \hat{H}_{MS}^{\mathrm{str}}] = 0$, the time evolution of this Hamiltonian can be written as a product of the gates driven on the two modes separately

$$\hat{U}_{MS}^{tot}(t) = \hat{\mathcal{D}}_{\text{com}}\left(\alpha_{\text{com}}(t)\hat{S}_{\varphi_1,\varphi_2}\right)\hat{\mathcal{D}}_{\text{str}}\left(\alpha_{\text{str}}(t)\hat{S}_{\varphi_1,\varphi_2}\right)e^{-i[\Phi_{\text{com}}(t)+\Phi_{\text{str}}(t)]\hat{S}^2_{\varphi_1,\varphi_2}}. \tag{4.29}$$

From the examples seen above, we know that the stretch mode will drive faster gates, with smaller α and Φ than the centre-of-mass mode. In the case of the square pulse, we can write down the equations

$$t_g = \frac{2\pi n}{\delta} = \frac{2\pi m}{\delta+\Delta},\ n, m \in \mathbb{Z} \tag{4.30}$$

$$\Phi_{\text{desired}} = 2\eta^2\Omega^2\left(\frac{1}{\delta} + \frac{1}{\delta+\Delta}\right)t_g, \tag{4.31}$$

which we can use to set t_g, δ, and Ω to reasonable values. As can be seen from the results of the simulation shown in Fig. 4.2 (where δ was set to $\Delta/5$, $t_g = 2\pi/\delta$, and Ω was chosen accordingly), this does solve the problem (the final fidelity is $> 99.99\%$), but the time interval where the state is near to the desired one is very narrower than in the ideal case, making the gate more sensitive to timing and intensity errors.

4.4.2 Motional Decoherence and Frequency Instability

From Eq. (4.16), (4.14), and (4.15) it is clear that any drift in motional frequency affects the outcome of the gate strongly, as it effectively changes the detuning δ. Moreover, the motion must be coherent throughout the gate time (since it is entangled with the two-qubit state), which implies that we are sensitive to both slow and fast (with respect to the gate time) noise on the motional frequency.

This kind of noise can be described by the Hamiltonian Eq. (4.8) (since the detuning is symmetric), but the time dependence of δ has an unknown component. In this discussion we are going to make the distinction between slow and fast noise, as they have different outcomes. Both effects follow from the statistical nature of expectation-value measurements[3] applied to different time scales.

The tool we use to study the consequences of both slow and fast noise is the so-called *Ramsey experiment* [32], which – as shown in figure 4.3 – consists of

[3] Averaging over a sufficient number of experiments (typically around 50) is necessary to obtain information about the expectation values, since single shots can only give boolean results.

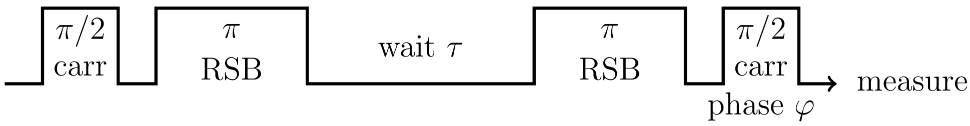

Figure 4.3: Pulse sequence for a Ramsey-type motional-coherence experiment.

- a carrier $\pi/2$ pulse mapping the initial state $|g,0\rangle$ to the superposition $(|g\rangle - i\,|e\rangle) \otimes |0\rangle / \sqrt{2}$,
- a red-sideband π pulse effectively mapping the superposition to the motional degree of freedom $|g\rangle \otimes (|0\rangle + |1\rangle)/\sqrt{2}$,
- a waiting time τ during which the two components of the state accumulate a random relative phase $|g\rangle \otimes (|0\rangle + e^{i\varphi_{\mathrm{deph}}}\,|1\rangle)/\sqrt{2}$ due to the motional phase noise,
- a red-sideband π pulse mapping the superposition back to the qubit degree of freedom $(|g\rangle + ie^{i\varphi_{\mathrm{deph}}}\,|e\rangle) \otimes |0\rangle / \sqrt{2}$,
- a carrier $\pi/2$ pulse with phase φ, producing (up to a global phase) the state $\left(\cos\left(\frac{\varphi_{\mathrm{deph}}-\varphi}{2}\right)|g\rangle + e^{i\varphi}\sin\left(\frac{\varphi_{\mathrm{deph}}-\varphi}{2}\right)|e\rangle\right) \otimes |0\rangle$,

where it is assumed that the rotating-wave approximation can be applied. The measured population of the excited state $|e\rangle$ for a given phase φ is going to be given by the average over n experiments of

$$P_{|e\rangle}(\varphi=\pi,\tau) = \sin^2\left(\frac{\varphi_{\mathrm{deph}}-\varphi}{2}\right) \tag{4.32}$$

$$= \frac{1}{2}\left[1-\cos(\varphi_{\mathrm{deph}}-\varphi)\right]. \tag{4.33}$$

If we assume φ_{deph} is normally distributed around zero with standard deviation $\sigma_\varphi(\tau)$, the expectation value $\lim_{n\to\infty}\overline{P_{|e\rangle}}(\varphi,\tau)$ is [32]

$$\lim_{n\to\infty}\overline{P_{|e\rangle}}(\varphi,\tau) = \frac{1}{2}\left(1-A\cos\varphi\right), \tag{4.34}$$

where the contrast A is given by

$$A = \int_{-\infty}^{\infty} \mathrm{d}\varphi_{\mathrm{deph}}\, e^{-\frac{\varphi_{\mathrm{deph}}^2}{2\sigma_\varphi^2}} \cos(\varphi_{\mathrm{deph}}) \tag{4.35}$$

$$= e^{-\frac{\sigma_\varphi^2}{2}}. \tag{4.36}$$

Note that this result is also a good approximation for any φ_{deph} symmetrically distributed around zero with a low probability of $\varphi_{\text{deph}}/\sigma_\varphi > 1$ [32].

Slow Motional-Frequency Noise

Slow drifts can be modelled by a (normally distributed with standard deviation σ_{slow}) random detuning δ_{slow} constant over the waiting time τ. Therefore, the phase φ_{deph} caused by δ_{slow} is going to be normally distributed with standard deviation $\sigma_{\text{slow}}\tau$, resulting into the following decay in contrast

$$A_{\text{slow}} = e^{-\frac{\sigma_{\text{slow}}^2 \tau^2}{2}}. \tag{4.37}$$

Fast Motional-Frequency Noise

In order to study the effect of fast noise, on the other hand, we represent the phase accumulation it causes as a random walk happening during the waiting time τ. Given Gaussian motional drifts we obtain a final phase normally distributed with standard deviation $\sigma_{\text{fast}}\sqrt{\tau}$, where σ_{fast} is proportional to the width of the frequency noise. This yields the contrast

$$A_{\text{fast}} = e^{-\frac{\sigma_{\text{fast}}^2 \tau}{2}}. \tag{4.38}$$

Effect of the Motional Dephasing on the MS Gate

The most straightforward way to study the effect of the decay in contrast shown by Eq. (4.37) and (4.38) on the MS gate is by adding a dephasing term to the master-equation solver used in the simulations. Even though this does not yield a complete picture of the consequences of motional frequency instability, it is useful to estimate the experimental requirements to this regard.

From the results of such simulations (which are shown in Fig. 4.4) it is clear that the motional phase-coherence time τ_{deph} must be at least a few hundreds of microseconds, in order not to reduce the MS gate fidelity below 99%.

Discriminating Between Slow and Fast Noise

Since the outcome of a Ramsey experiment shows the combined effect of the slow and fast drifts, it is not always possible to determine the extent to which the two kinds of noise contribute to the motional dephasing based on this experiment alone. However, it is important to be able to make this distinction, as it helps to direct our experimental efforts.

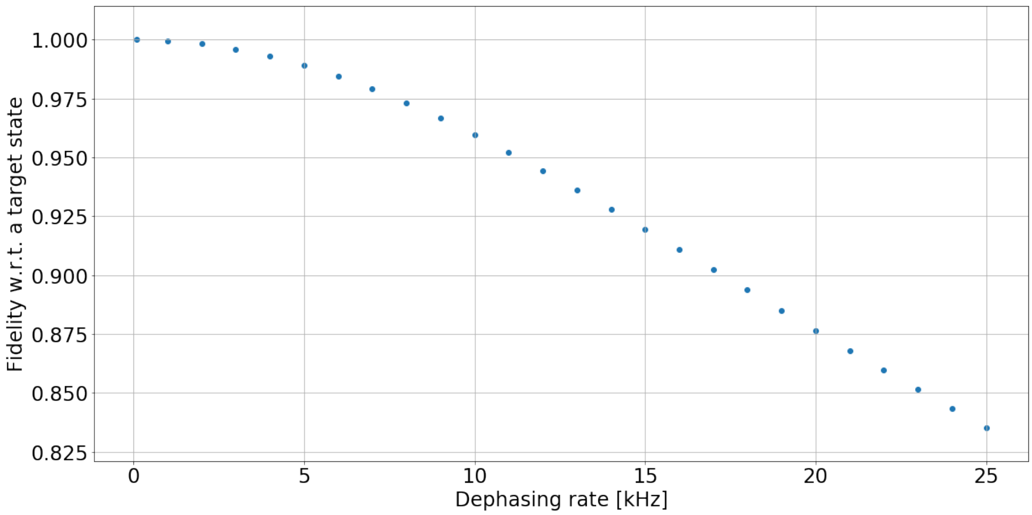

Figure 4.4: Simulated dependence of the fidelity w.r.t. a target state on the dephasing rate τ_{deph}^{-1}.

This issue can be solved by additionally performing a Ramsey experiment with motional spin echo, which consists of the addition of a carrier π pulse "sandwiched" between two red-sideband π pulses in the middle of the wait time. Tracking the state evolution over this experiment yields:

- carrier $\pi/2$: $(\left|g\right\rangle - i\left|e\right\rangle) \otimes \left|0\right\rangle/\sqrt{2}$,
- red-sideband π: $\left|g\right\rangle \otimes (\left|0\right\rangle + \left|1\right\rangle)/\sqrt{2}$,
- waiting time $\tau/2$: $\left|g\right\rangle \otimes (\left|0\right\rangle + e^{i(\delta_{\text{slow}}\tau/2+\varphi_{\text{fast}}^{(1)})}\left|1\right\rangle)/\sqrt{2}$,
- echo pulses: $\left|g\right\rangle \otimes (e^{i(\delta_{\text{slow}}\tau/2+\varphi_{\text{fast}}^{(1)})}\left|0\right\rangle + \left|1\right\rangle)/\sqrt{2}$
- waiting time $\tau/2$: $\left|g\right\rangle \otimes (e^{i(\delta_{\text{slow}}\tau/2+\varphi_{\text{fast}}^{(1)})}\left|0\right\rangle + e^{i(\delta_{\text{slow}}\tau/2+\varphi_{\text{fast}}^{(2)})}\left|1\right\rangle)/\sqrt{2}$
- red-sideband π: $e^{i(\delta_{\text{slow}}\tau/2+\varphi_{\text{fast}}^{(1)})}(\left|g\right\rangle + ie^{i(\varphi_{\text{fast}}^{(2)}-\varphi_{\text{fast}}^{(1)})}\left|e\right\rangle) \otimes \left|0\right\rangle/\sqrt{2}$,
- carrier $\pi/2$ with phase φ: $\left(\cos\left(\frac{\varphi_{\text{fast}}-\varphi}{2}\right)\left|g\right\rangle + e^{i\varphi}\sin\left(\frac{\varphi_{\text{fast}}-\varphi}{2}\right)\left|e\right\rangle\right) \otimes \left|0\right\rangle$

where $\varphi_{\text{fast}}^{(1)}, \varphi_{\text{fast}}^{(2)}$ are the random phases accumulated during the first and the second waiting time, respectively, $\varphi_{\text{fast}} = \varphi_{\text{fast}}^{(2)} - \varphi_{\text{fast}}^{(1)}$, and the global phase was neglected in the last step. It is clear that the "population inversion" operated by the echo pulses effectively nullifies the action of slow drifts and leaves us with the fast noise alone. A more detailed discussion about the further informations that one can obtain with this technique is given in [33].

Improving the Motional Frequency Stability

From Eq. (2.34) it follows that the experimental parameters on which the radial mode frequencies depend are the static voltage applied in the axial direction, and the amplitude and frequency of the oscillating radial potential. From the characteristics of our experimental apparatus, it turns out that the main source of error among these quantities is the amplitude of the rf potential, which did not require stabilisation before the experiments attempted in this thesis. Therefore, after the theoretical analysis the focus was moved onto the rf stabilisation. Due to unexpected technical difficulties, the latter turned out to be the main work of this thesis, and is thus described in a dedicated chapter (Chap. 6).

Chapter 5

Transport Gates

As previously mentioned, one of the main issues on the way towards the production of a serviceable quantum computer is the scalability of the device. In this chapter I will introduce transport gates, argue why they are valuable from the perspective of scalability, discuss the implementation of transport MS gates, and study the related experimental issues.

5.1 Working Mechanism

The idea behind transport gates is fairly simple: in principle, in the frame of reference of the qubit there is no difference between a laser pulse being applied to an ion and the ion itself travelling through a constantly-on laser beam, therefore it is possible to implement gates based on the transport [6]. This can be beneficial, in that it allows the transfer of part of the experimental complexity from the optics to the electronics. Indeed, in this kind of gate the pulse timing is handled by the dc electrodes of the Paul trap, which are technically simpler to characterise and operate than the AOMs. As a motivation, it is worth stressing that AOMs are challenging devices to employ, as their behaviour (including response time and conversion efficiency) varies strongly depending on their model and alignment, to the point where the reproducibility of the experiments in which they are used might be compromised.

Furthermore, combining the transport-gate principle to the segmented-trap architecture enables the recycling of the laser beams by reflecting them back into different trap zones, thereby improving the scalability of the optical apparatus [6, 7].

However, transporting the ions without spoiling their motional coherence is not trivial, as they should "perceive" the same environment throughout the

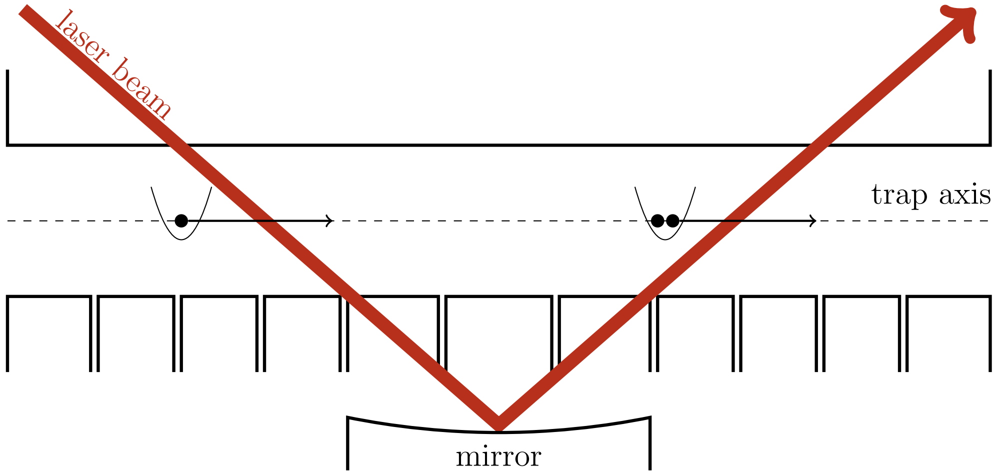

Figure 5.1: Illustration of parallel transport gates on a segmented trap setup. The scale and the number of electrodes are not realistic.

duration of the transport. This is implemented by changing the potentials applied to the dc electrodes such that the potential well in which the ion is trapped moves at a constant velocity along the axis, as described in [14]. Due to experimental imperfections, it is impossible to guarantee completely constant velocity and axial confinement strength. Therefore, exploiting the axial mode of motion is problematic for two reasons. First of all, the motional frequency would not be constant. Secondly, in order to couple to this mode, the effective wave vector $\vec{k}$ would have to point in the axial direction, resulting in a large and time-dependent Doppler shift (which is given by the scalar product of $\vec{k}$ and the transport velocity). Since both these problems can be significantly reduced by working with the radial modes, we decided to employ the latter for this thesis.

5.2 Laser-Ion Interaction During Transport

The laser-ion interaction of an ion trapped in a potential well moving with velocity $\vec{v}_{\mathrm{w}}(t)$ can be described by transforming to the co-moving frame of the trapping potential. This leads to rewriting every velocity- and space-dependent quantity as a time-dependent parameter by inserting the velocity $\vec{v}_{\mathrm{w}}(t)$ and position $\vec{r}_{\mathrm{w}}(t) = \vec{r}_{\mathrm{w}0} + \int_{t_0}^{t} \mathrm{d}t' \vec{v}_{\mathrm{w}}(t')$ of the well into the laser-ion interaction Hamiltonian, obtaining

$$\hat{H}_I = \frac{\hbar\Omega(t)}{2} \left(e^{i[\vec{k}_l \cdot \hat{\vec{r}} - (\omega_{eg} - \omega_l - \delta_D(t) + \delta_S(t))t + \varphi]} \hat{\sigma}_+ + H.c. \right), \tag{5.1}$$

where $\hat{\vec{r}}$ is the position operator of the ion in the moving well, $\Omega(t)$ is proportional to the laser intensity at the position, $\vec{r}_\mathrm{w}(t)$, $\delta_D(t) = \vec{k}_l \cdot \vec{v}_\mathrm{w}(t)$ takes into account the Doppler shift due to the transport, and $\delta_S(t) \propto \Omega(t)$ is the AC Stark shift induced by the Raman beams. Since the beams we use are to a good approximation Gaussian and the velocity fluctuates by only around 1% in time, we will treat $\Omega(t)$ as a Gaussian "pulse".

Apart from the Doppler and the AC Stark shift, this Hamiltonian is equivalent to the one given by Eq. (3.11) and can be expanded in the Lamb-Dicke approximation to obtain a very similar form to Eq. (3.34). Note that the AC Stark shift is present in the case of standard gates as well, but it has been neglected in Chap. 4 because in the square-pulse MS gate it is constant and can therefore be compensated by tuning the centre laser frequency ω_l.

5.3 The Transport Mølmer Sørensen Gate

Since the Doppler and the AC Stark shift act on the carrier frequency, they add an asymmetric component to the detuning δ used in the MS gate

$$\delta_{RSB}(t) = \delta + \delta_D(t) + \delta_S(t), \tag{5.2}$$

$$\delta_{BSB}(t) = -\delta + \delta_D(t) + \delta_S(t), \tag{5.3}$$

therefore we need to neglect them at first in order to be able to use the results from Sec. 4.3. They are investigated with the help of simulations in Sec. 5.4. As mentioned in Sec. 5.2, the transport of the ions through the laser beam can be modelled as a Gaussian pulse

$$\delta \equiv \text{const},\ \Omega(t) = \Omega_0 e^{-\frac{(t-t_0)^2}{\tau^2}}. \tag{5.4}$$

Despite the Gaussian distribution being an excellent approximation for the physical pulse shape and a very powerful mathematical tool (being analytic), it has a very un-physical property: it is never zero. Thus, it does not make sense to interpret the gate time t_g as the time over which one integrates to obtain α and Φ. Rather, we are going to integrate over the entire domain $\mathbb{R}$ and use the pulse width τ as an equivalent parameter to t_g, which is consistent with the fact that the physical situation implies a pulse with a finite support

$$\alpha = -i\frac{\eta\Omega_0}{2}\int_{-\infty}^{+\infty} \mathrm{d}t\, e^{-\frac{t^2}{\tau^2}+i\delta t}, \tag{5.5}$$

$$\Phi = \frac{\eta^2\Omega_0^2}{4}\int_{-\infty}^{+\infty} \mathrm{d}t \int_{-\infty}^{t} \mathrm{d}t'\, e^{-\frac{t^2+t'^2}{\tau^2}} \sin(\delta t - \delta t'). \tag{5.6}$$

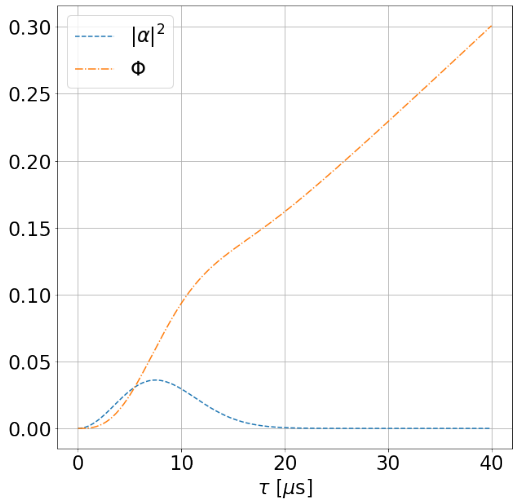

Figure 5.2: Dependence of $|\alpha|$ and Φ for a Gaussian pulse on the pulse width τ (which corresponds to the gate time in a square gate).

The integral for α is straightforward to evaluate, and the one for Φ can be solved by substituting $2i\sin(\delta t - \delta t') = e^{i\delta(t-t')} - e^{-i\delta(t-t')}$ and transforming to rotated coordinates $u = (t+t')/\sqrt{2}$ and $v = (t-t')/\sqrt{2}$ in order to obtain two independent integrals [6]

$$\alpha = -i\frac{\sqrt{\pi}}{2}\eta\Omega_0\tau e^{-\frac{\delta^2\tau^2}{4}}, \tag{5.7}$$

$$\begin{aligned}\Phi &= \frac{\eta^2\Omega_0^2}{8i}\left(\int_{-\infty}^{+\infty} \mathrm{d}u\, e^{-\frac{u^2}{\tau^2}} \int_{0}^{+\infty} \mathrm{d}v\, e^{-\frac{v^2}{\tau^2}+i\sqrt{2}\delta v} - \int_{-\infty}^{+\infty} \mathrm{d}u\, e^{-\frac{u^2}{\tau^2}} \int_{0}^{+\infty} \mathrm{d}v\, e^{-\frac{v^2}{\tau^2}-i\sqrt{2}\delta v}\right) \\ &= \frac{\pi}{4}\eta^2\Omega_0^2\tau^2 e^{-\frac{\delta^2\tau^2}{2}}\mathrm{erfi}\left(\frac{\delta\tau}{\sqrt{2}}\right) = -\alpha^2\mathrm{erfi}\left(\frac{\delta\tau}{\sqrt{2}}\right),\end{aligned} \tag{5.8}$$

where we used the identity $\mathrm{erf}(iz)/i = \mathrm{erfi}(z)$. One must be careful with the imaginary error function erfi, as it does not saturate to a fixed value like its real counterpart does. Indeed, as plotted in Fig. 5.2, erfi grows rapidly enough to compensate for the decay term $e^{-\delta^2\tau^2/2}$ and leads to asymptotic linear behaviour, consistent with the intuition about the effect of a longer gate time that one gets from the treatment of the square-pulse case.

The trajectory in the motional phase-space can be obtained by integrating α from $-\infty$ to the time t, which yields the expression

$$\alpha(t) = \sqrt{\pi}\eta\Omega_0\tau e^{-\frac{\delta^2\tau^2}{4}}\frac{\mathrm{erf}\left(\frac{t}{\tau} - i\frac{\delta\tau}{2}\right)+1}{2}, \tag{5.9}$$

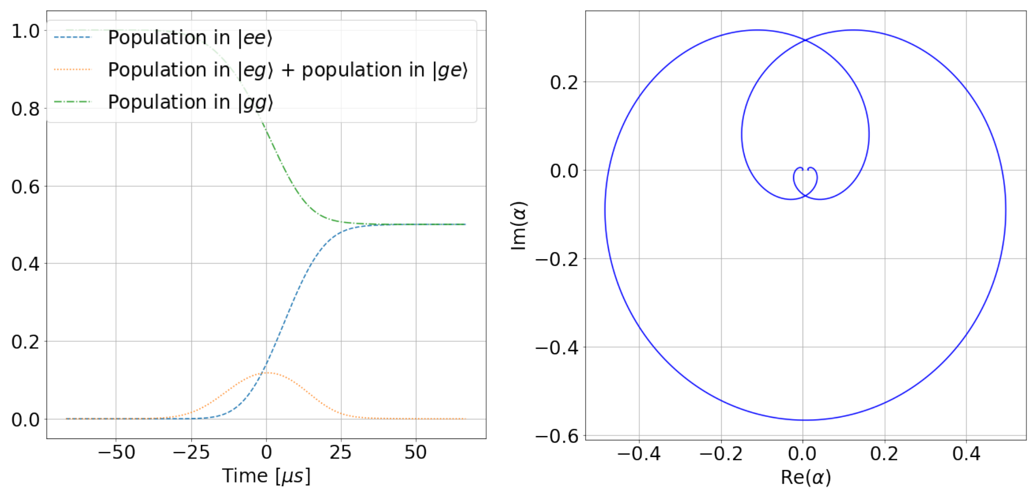

Figure 5.3: Reference traces for the simulated results of the ideal case of an MS gate with a Gaussian pulse. The left plot shows the time evolution of the two-qubit populations. The right plot shows the motional phase-space trajectory, i.e. the path followed by $\alpha(t)$ starting from zero.

which can only be evaluated numerically, and for which some example plots can be found in [6].

5.4 Error Sources and Experimental Issues

As mentioned above, the transport version of the MS gate introduces new experimental difficulties with respect to the standard one. In this section I will discuss how such effects affect the gate and the possible methods of reducing their influence.

Fig. 5.3 shows the simulation of an ideal MS gate with a Gaussian pulse. The final fidelity with respect to the target state in this case is 99.99%, and could be further improved by a systematic computer optimisation of the experimental parameters.

5.4.1 Delay between the Ions

An issue not previously discussed is that the ions travel through the beam with a significant delay with respect to each other. Indeed, from equation Eq. (2.41) we find that they are going to be spaced by approximately 5 μm, which is a relevant fraction of the typical beam waist 30 μm.

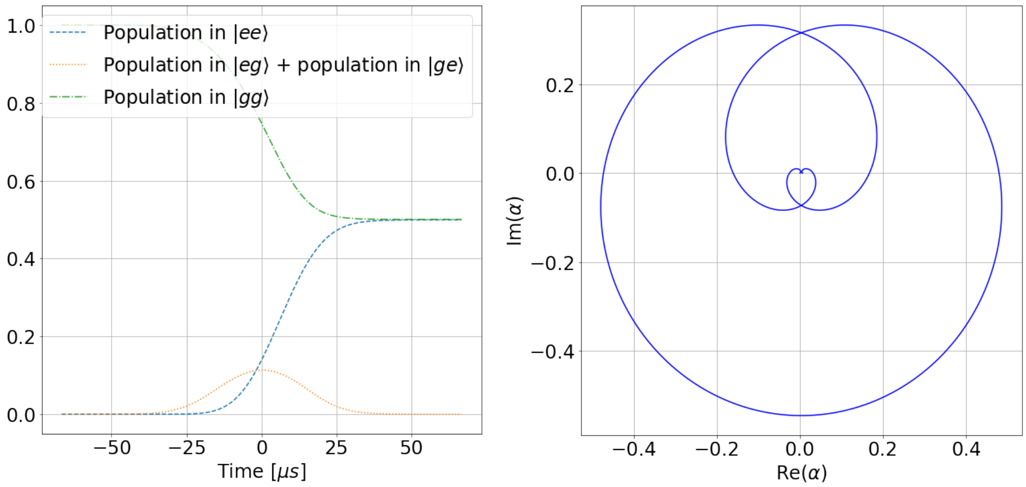

Figure 5.4: Simulated time evolution of the populations (left) and phase-space trajectory (right) for the transport MS gate when taking into account the delay between the ions. It is clear that adjusting the experimental parameters is enough to compensate for this effect.

To quantify the impact of this effect, we can calculate the time evolution of the gate with two different intensity profiles for the two ions $\Omega_1(t), \Omega_2(t)$ and equal detuning $\delta(t)$

$$\hat{H}_{MS}^{delay}(t) = \frac{\hbar\eta}{2}\left(e^{i\delta(t)t}\hat{a} + e^{-i\delta(t)t}\hat{a}^\dagger\right)\left(\Omega_1(t)\hat{\sigma}_{\varphi_1}^{(1)} + \Omega_2(t)\hat{\sigma}_{\varphi_2}^{(2)}\right), \tag{5.10}$$

from which we can calculate the time evolution of the system in the same way as in Sec. 4.3

$$\hat{U}_{MS}^{delay}(t) = \hat{\mathcal{D}}\left(\alpha_1(t)\hat{\sigma}_{\varphi_1}^{(1)} + \alpha_2(t)\hat{\sigma}_{\varphi_2}^{(2)}\right) e^{-i\hat{\Gamma}_{\varphi_1,\varphi_2}(t)}, \tag{5.11}$$

where

$$\alpha_j(t) = -i\frac{\eta}{2}\int_{t_0}^{t} \mathrm{d}t'\Omega_j(t')e^{i\delta(t')t'},\ j \in \{1,2\}, \tag{5.12}$$

$$\begin{aligned}\hat{\Gamma}_{\varphi_1,\varphi_2}(t) = \frac{\eta^2}{4}\int_{t_0}^{t}\mathrm{d}t'\int_{t_0}^{t_1}\mathrm{d}t''\sin(\delta(t')t' - \delta(t'')t'') \\ \times (\Omega_1(t')\hat{\sigma}_{\varphi_1}^{(1)} + \Omega_2(t')\hat{\sigma}_{\varphi_2}^{(2)})(\Omega_1(t'')\hat{\sigma}_{\varphi_1}^{(1)} + \Omega_2(t'')\hat{\sigma}_{\varphi_2}^{(2)}).\end{aligned} \tag{5.13}$$

Given that in our case $\Omega_1(t)$ and $\Omega_2(t)$ are Gaussian profiles with $\Omega_1(t) = \Omega_2(t + \Delta t)$ (where Δt is the delay) and that the effect of the gate for a

Gaussian pulse is given by the limit $t_0 \to -\infty, t \to \infty$, it follows that

$$\alpha_1 = -i\frac{\eta\Omega_0}{2}\int_{-\infty}^{\infty} \mathrm{d}t\, e^{-\frac{t^2}{\tau^2} i\delta t} = -i\frac{\eta\Omega_0}{2}\int_{-\infty}^{\infty} \mathrm{d}t\, e^{-\frac{(t+\Delta t)^2}{\tau^2} i\delta t} = \alpha_2, \tag{5.14}$$

therefore the final motional state is unaffected by the delay. Regarding $\hat{\Gamma}_{\varphi_1,\varphi_2}$, some intuition about its form can be acquired by examining the terms in its integral. For instance, $\Omega_1(t')\Omega_1(t'')(\hat{\sigma}^{(1)}_{\varphi_1})^2$ and $\Omega_2(t')\Omega_2(t'')(\hat{\sigma}^{(2)}_{\varphi_2})^2$ can be integrated as in the ideal case and yield $2\Phi\hat{\mathbb{I}}$, where Φ is given by Eq.(5.8). The remaining two terms (which are mathematically challenging to evaluate explicitly) give a reduced contribution because of the smaller overlap between the two Gaussian profiles, resulting in something of the form $\tilde{\Phi}\hat{\sigma}^{(1)}_{\varphi_1}\hat{\sigma}^{(2)}_{\varphi_2}$, where $\tilde{\Phi} = \Phi$ for $\Delta t = 0$ and $\tilde{\Phi} \to 0$ for $\Delta t \gg \tau$. This implies that

$$\lim_{\Delta t \to 0} \hat{\Gamma}_{\varphi_1,\varphi_2} = \Phi \hat{S}^2_{\varphi_1,\varphi_2}, \tag{5.15}$$

$$\lim_{\Delta t/\tau \to \infty} \hat{\Gamma}_{\varphi_1,\varphi_2} = 2\Phi\hat{\mathbb{I}}, \tag{5.16}$$

which is equivalent to stating that for vanishing delay the ideal MS gate is recovered, and that the state-dependent phase accumulation is weakened by Δt to the point that it gets reduced to a global phase when the ions are very far apart.

This was confirmed by the simulation shown in Fig. 5.4, from which it was found that for our experimental parameters the ideal-case fidelity can be recovered by slightly decreasing the transport velocity – i.e. by increasing the effective gate time in order to compensate for the weakening of the state-dependent phase accumulation.

5.4.2 AC Stark Shift

Since the beryllium qubit is driven by Raman transitions, we need to take into account the AC Stark shift caused by the off-resonant coupling to the adiabatically eliminated state. We must however be careful, because the model we used in Sec. 3.3 is highly simplified. Since $\Delta \gg \omega_{eg}$, it is clear that both drive lasers will off-resonantly couple both qubit states to $|f\rangle$, inducing additional AC Stark shifts. In addition to this, the state $|f\rangle$ belongs to a set of closely-lying $P_{1/2}$ levels, and it is not the only one with an allowed dipole transition to the qubit states. Therefore – even though the two-photon Raman transition is adequately described in Sec. 3.3 – the AC Stark shift on the qubit levels contains several contributions from other off-resonant transitions

$$\delta_S = \sum_{l\in\{\text{co,sw}\}} \sum_{|f\rangle\in P_{1/2}} \left(\frac{{\Omega_{fg}^{(l)}}^2}{4(\omega_{fg}-\omega_l)} - \frac{{\Omega_{fe}^{(l)}}^2}{4(\omega_{fe}-\omega_l)} \right), \tag{5.17}$$

where $\Omega_{ij}^{(l)}$ is the Rabi frequency associated with the coupling between the states $|i\rangle$ and $|j\rangle$ by the laser l – thus it is proportional to the product between the matrix element of the transition and the laser intensity. Note that this expression depends strongly on the polarisation of light which can be engineered to reduce δ_S effectively [6]. A detailed discussion about AC Stark shifts in hyperfine qubits is given in [20].

Since δ_S depends strongly on the involved state, it is expected to be different between the FDQ and the FIQ transitions. Indeed, on the FDQ it is stronger, thus contributing to the FIQ being a more desirable qubit choice. This property of the FIQ implies that the qubit states receive similar total shifts, and it turns out that this is also valid when applying only one of the two Raman lasers, making this feature insensitive to power imbalance between the two beams [12].

Given that the beam centres of the two Raman lasers are close to each other, in the simulations the AC Stark shift was approximated as being proportional to the effective Rabi frequency of the induced transition, which is given by the Gaussian

$$\delta_S(t) = \delta_{S0} e^{\frac{(t-t_0)^2}{\tau^2}} \propto \Omega(t) = \frac{\Omega_g(t)\Omega_e(t)}{4\Delta} = \Omega_0 e^{\frac{(t-t_0)^2}{\tau^2}}, \tag{5.18}$$

where

$$\Omega_0 = \frac{\Omega_g^0 \Omega_e^0}{4\Delta} e^{-(t_g^0-t_e^0)^2},\ t_0 = \frac{\tau_g^2 t_e^0 + \tau_e^2 t_g^0}{\tau_g^2+\tau_e^2},\ \tau = \frac{\tau_g\tau_e}{\sqrt{\tau_g^2+\tau_e^2}}, \tag{5.19}$$

and where Ω_l^0 is the maximum Rabi frequency, t_l^0 the effective pulse centre (i.e. the instant at which the ion travels through the beam centre), and τ_l the effective pulse width (i.e. the time the ion takes to travel through the beam waist) of laser $l \in \{g, e\}$.

There are several techniques applied to compensate for the AC Stark shift, which are only mentioned here and discussed in detail in the literature. They can be divided into two categories; one aims to actively correct for the detuning in real time. This can be done either by keeping track of the detuning over time and compensating for it with laser pulses (which is useless for MS gates, where the main problem is the asymmetric detuning), or by tuning the carrier frequency in real time, which would however nullify two

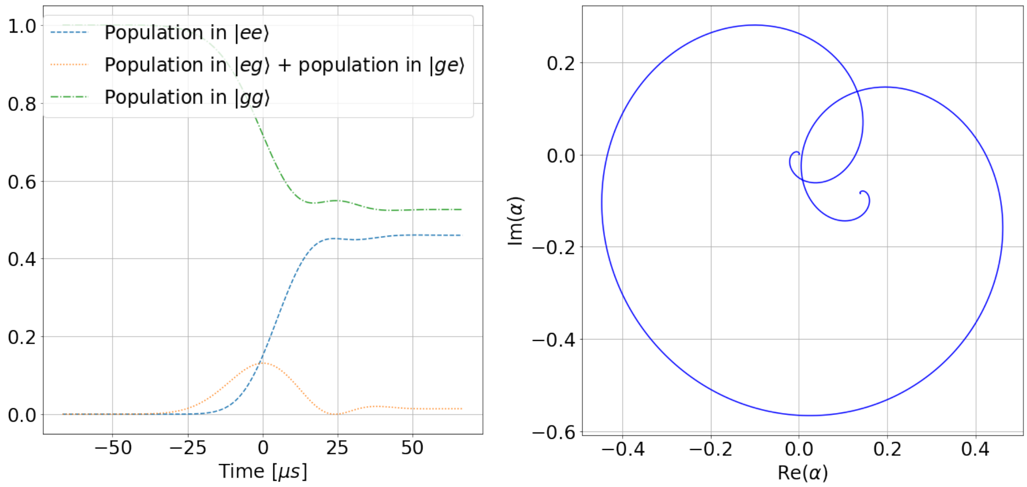

Figure 5.5: Simulated effect of the AC Stark shift (with maximum shift 3 kHz) on the Gaussian-pulse MS gate.

of the reasons to use transport gates, since the timing would become more complicated than with standard gates, and realising parallel gates in the same beam would become very difficult. The techniques of the second kind, on the other hand, consist in engineering the laser configuration so that the terms in Eq. (5.17) compensate each other, which has the advantage of being independent of the laser intensity. To provide an example, in [6] this is done by selecting the beam polarisations.

In our case we plan to use the FIQ transition, where the contributions to the AC Stark effect partly compensate each other. Nevertheless, this is not sufficient to make it a negligible error source. Indeed, from the simulations shown in Fig. 5.5 it can be concluded that for a maximum shift of 3 kHz (which is the worst-case scenario we observed in the lab) we obtain a gate infidelity around 2% and a non-negligible entanglement to the motion. Thus, in order to obtain a high-fidelity gate, it will be necessary to further reduce the effects of the AC Stark shift. A proposal is formulated in Sec. 5.4.4.

5.4.3 Doppler Shift

The Hamiltonian given in Eq. (5.1) includes the Doppler shift $\delta_D = \vec{k}_l \cdot \vec{v}$, where $\vec{v}$ is the transport velocity. This shift describes the change in observed light wavelength in the moving frame of the ions. It effectively shifts the carrier frequency, thereby causing an asymmetric detuning in the MS gate.

The strength of the Doppler shift depends on two experimental imperfections, namely the laser misalignment with respect to the trap axis and the time-dependent velocity. Indeed, if the alignment were perfect, in the co-90-new beam configuration $\vec{k}_l$ would be perpendicular to $\vec{v}$ with an angular imprecision on the order of 10^{-6} rad, leading to a negligible effect. Furthermore, if the velocity were constant, δ_D would be constant as well, thus it could be compensated by calibrating the carrier frequency with a corresponding offset.

In the following it is advantageous to define the angle $\theta = \vec{k}_l \sphericalangle \vec{v} - \pi/2$, and to split the velocity into a constant and a time-dependent component $\vec{v}(t) = \vec{v}_0 + \vec{v}'(t)$. Since $\vec{v}$ is purely in axial direction, we can treat it as a scalar function, obtaining

$$\delta_D = \frac{2\pi}{\lambda_l}[v_0 + v'(t)] \sin\theta = \delta_D^0 + \delta'_D(t), \tag{5.20}$$

where $\lambda_l = 2\pi/|\vec{k}_l|$ is the wavelength of the effective wave vector of the Raman transition. It is worth noting that the constant component of δ_D can indeed be compensated with proper laser calibration, thus we can reduce our focus on $\delta'_D(t)$.

From the results of [34] we assume that on our apparatus the time dependence can be approximated to first order as parabolic, with the minimum velocity at the beam centre

$$v'(t) = v_1(t - t_0)^2, \tag{5.21}$$

where t_0 is the instant at which the ion travels through the beam centre. Thus the time-dependent component of the Doppler shift is given by

$$\delta'_D(t) = \delta_D^1(t - t_0)^2,\ \delta_D^1 = \frac{2\pi v_1}{\lambda_l}\sin\theta. \tag{5.22}$$

The sign of the Doppler shift depends on the sign of the angle θ, and its effect on the MS gate is not symmetric around $\theta = 0$, as shown in Fig 5.6. The asymmetry is mainly due to the fact that the phase-space trajectory leads to a better disentanglement from the motion in the case of negative θ, as shown in Fig. 5.7.

It is worth mentioning that since the publication of [34] the time-dependent component of the velocity has been reduced to approximately 1% of the total [14]. This implies that the effective pulse profile in the frame of reference of the ion is still Gaussian to a very good approximation, therefore the time-dependent Doppler shift is the only effect of the non-constant velocity that cannot be corrected by tuning the gate time, laser intensity, and detuning.

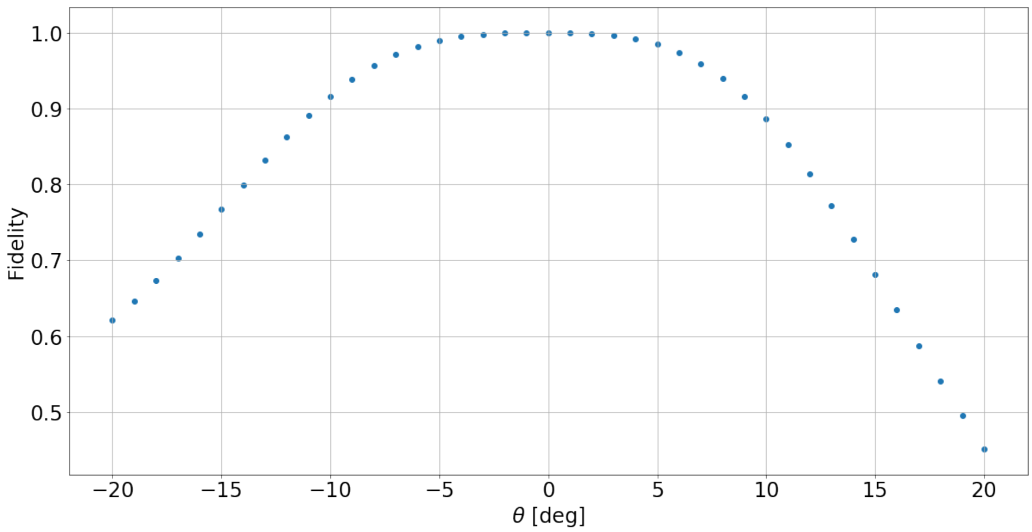

Figure 5.6: The fidelity of the MS gate with a Gaussian pulse as a function of the beam misalignment. The Doppler shift is the only effect considered here.

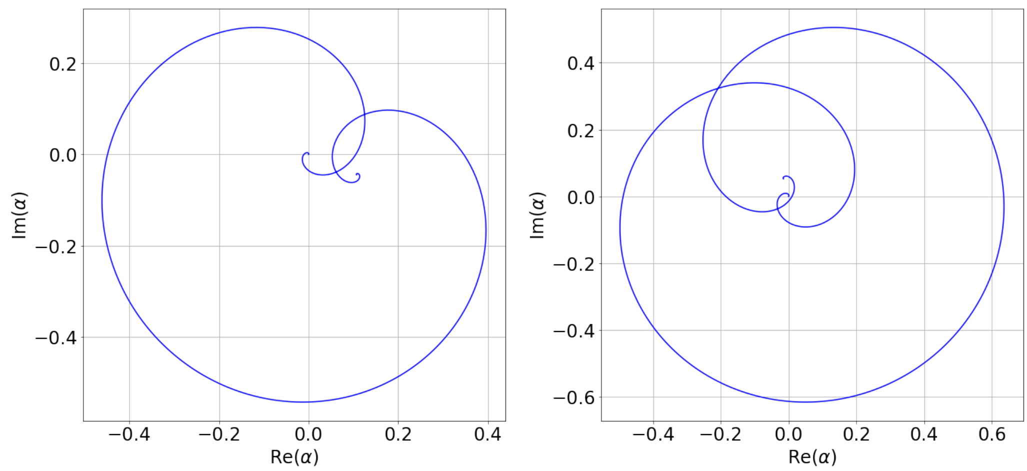

Figure 5.7: Comparison of the effect of the Doppler shift on the phase-space trajectory for $\theta = +5°$ (left) and $\theta = -5°$ (right). The difference between these trajectories explains the asymmetry in θ of the fidelity shown in Fig. 5.6.

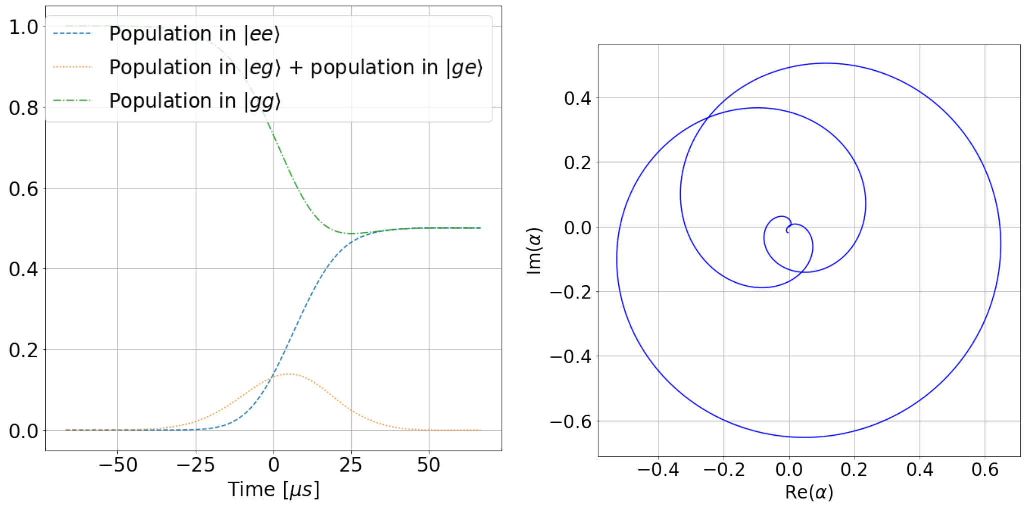

Figure 5.8: Simulated effect of competing AC Stark and Doppler shift. The left plot shows the time evolution of the measurable populations, and the phase-space trajectory $\alpha(t)$ is shown on the right..

5.4.4 Competing Doppler and AC Stark shift

The possibility of obtaining different signs for δ_D by modifying the alignment of the apparatus implies that we can set up the experiment so that the Doppler and the AC Stark shift give opposite contributions. Since they have different time profiles, they cannot compensate for each other completely, but by tuning the experimental parameters one can achieve at least a fidelity of 99.9%, as shown in Fig. 5.8. This is a significant improvement with respect to the case where only one of these effects is considered, where the fidelity is typically 98%.

The one based exclusively on the angle θ is not a reliable and flexible method, as it requires changing the alignment of the optical apparatus with great precision every time the laser power alters. However, it is in principle possible to modify the transport waveforms to systematically match the profile of $\delta_D(t)$ to $\delta_S(t)$, which can potentially recover the loss in fidelity due to the time-dependent AC Stark shift.

Chapter 6

The RF Stabilisation

As discussed in Sec. 4.4.2, it is crucial for the purpose of this thesis to have a stable radial motional frequency, and the level of stability is a new requirement for our apparatus. As mentioned at the end of Sec. 4.4.2, the only parameters contained in Eq. (2.34) that can vary over time are the dc potential applied in the axial direction, and the amplitude and frequency of the radial rf potential. Regarding the dc potential, it is stable enough to enable the encoding of a qubit in the axial motional state [29] with calcium ions, which is more than enough for our needs. The effect of a rf frequency oscillation $\delta\omega_{\text{rf}}$ on the radial frequency is suppressed by $\mathcal{O}(\delta\omega_{\text{rf}}/\omega_{\text{rf}})$, thus it is totally negligible – moreover ω_{rf} drifts by a few hundred Hz over several hours. Therefore, the only remaining quantity to stabilise is the amplitude of the rf voltage.

Note that the statement about the dc stability is not valid in the case of transport gates – as experimental imperfections cause the axial confinement to vary over time. However, a fractional change in the dc voltage influences the radial frequency approximately ten times less than the same fractional change in the rf amplitude. Moreover, given the properties of the apparatus, we expect the fractional changes of the static potential to be significantly smaller than the ones of the rf amplitude before stabilisation.

6.1 The RF Circuit

The way the rf voltage is generated is depicted in Fig. 6.1, and the components of the circuit are listed in Tab. 6.1. Many of the small parts are grouped in the so-called *rf box*, as noted in Fig. 6.1. I will explain the system step by step, starting from the top left in Fig. 6.1.

- The signal is produced by a rf generator.

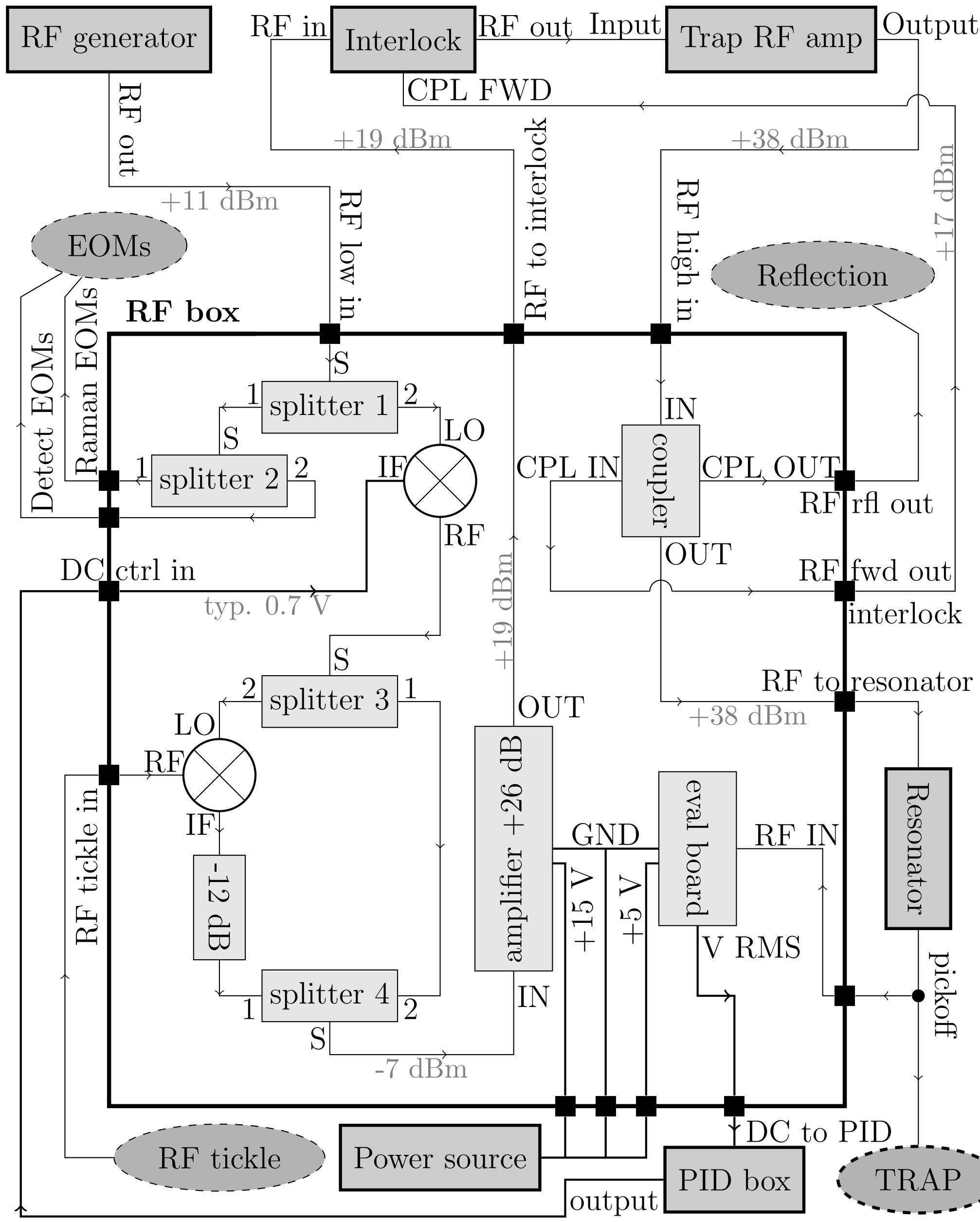

Figure 6.1: Schematic of the rf circuit. Thin lines represent rf-signal transmission, thick lines are used for dc voltages, the thicker rectangle denotes the rf box, and black squares indicate ports on the rf box. The components are listed in Tab. 6.1. The labels written near the ports correspond to the ones currently present in the apparatus. A detailed explanation of the circuit can be found in the text.

Splitters 1 & 3	Mini-Circuits ZFSC-2-4-S+
Splitters 2 & 4	Mini-Circuits ZMSC-2-1+
First mixer	Mini-Circuits ZLW-3+
Second mixer	Mini-Circuits ZX05-1L-S+
Coupler	Mini-Circuits ZFDC-20-1H-S+
Attenuators	Mini-Circuits MCL VAT-xW2+ where x = attenuation value
Amplifier	Mini-Circuits ZFL-1000VH2
Eval board	Analog Devices ADL5511
RF generator	Rohde & Schwarz SMC100A
Trap RF amp	Mini-Circuits TIA-1000-4
PID box	Newport New Focus LB1005

Table 6.1: Components of the rf circuit pictured in Fig. 6.1.

- The splitters 1 and 2 distribute part of the signal to the EOMs that are used to compensate for the frequency modulation due to the micromotion of beryllium. It is important to use a signal from the same source, because the phase between micromotion and compensation must be fixed.

- The first mixer after splitter 2 modulates the signal amplitude based on the dc voltage which the output of a PID controller applies to its IF input. This is how the amplitude stabilisation is applied.

- Between splitter 3 and 4 an additional rf signal (at a few MHz) is added to the main one. It is called the *rf tickle*, and can be used for example to find the frequency of the radial modes of motion without laser manipulations. This is however impossible with beryllium, because the tickle generation circuit cannot reach high enough frequencies.

- The signal passes through an initial amplification stage (at low power, around 100 mW) and is fed to an interlock, which can interrupt the circuit whenever the amplitude exceeds a set limit.

- After the interlock, the signal is amplified further, reaching a power on the order of 10 W.

- A bidirectional coupler is used for monitoring the signal going to the trap (CPL IN) and the reflection (CPL OUT). Normally, both should be fed to the interlock CPL FWD and CPL RFL ports respectively,

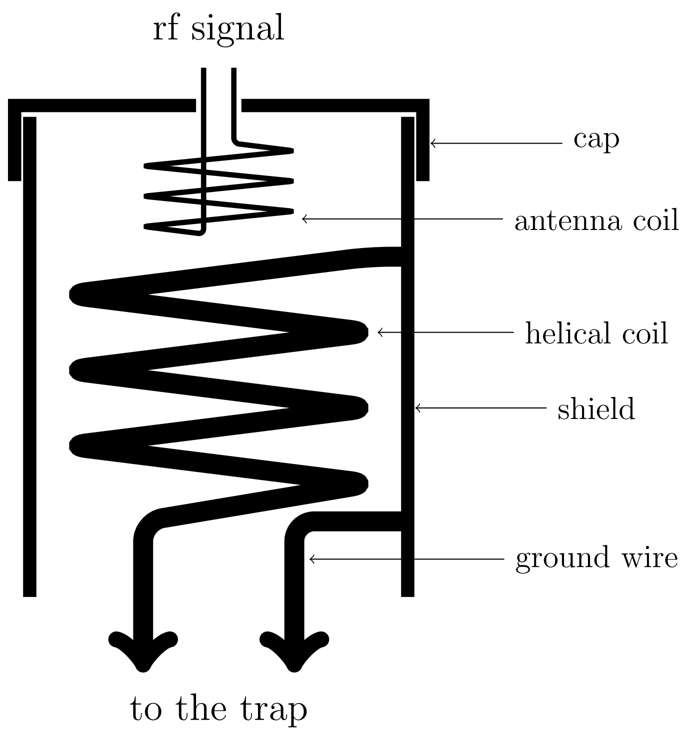

Figure 6.2: Schematic of a helical resonator.

but the reflection is instead often monitored with a spectrum analyser in order to optimise impedance matching.

- A helical resonator couples the signal into the trap. Its main effects are: increasing the voltage amplitude of the signal, applying additional frequency and noise filtering, and simplifying impedance matching.
- A small fraction of the signal after the resonator is picked off using a capacitive divider and is fed into an evaluation board that returns its RMS amplitude. The amplitude is then stabilised by a PID controller feeding back on the first mixer.

More details about the parts of the circuit that are not treated extensively in this thesis can be found in [13, 12].

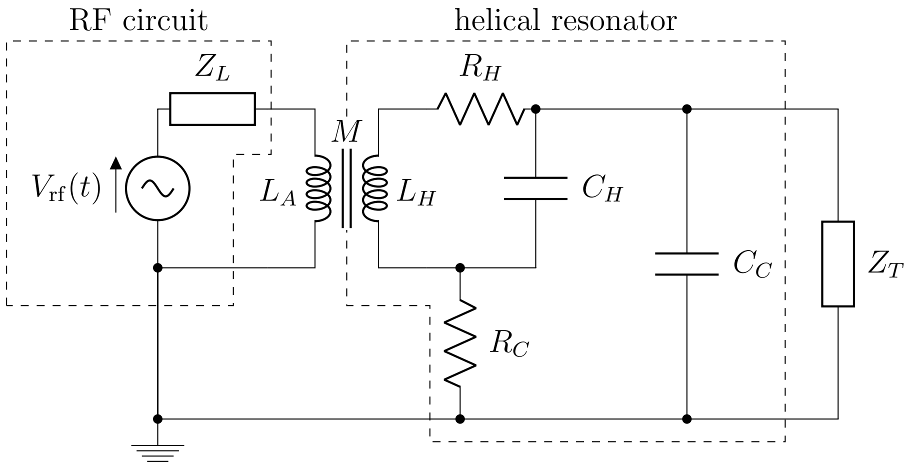

Figure 6.3: Lumped-circuit model for a helical resonator, where Z_L represents the impedance of the transmission line (usually 50 Ω), L_A and L_H the inductances of the antenna and the helical coil, M the inductive coupling between them, R_H the resistance of the helix, C_H the self-capacitance of the helix, C_C the shield-to-helix capacitance, R_C the shield resistance plus the shield-helix one, and Z_T the complex impedance of the trap.

6.2 The Helical Resonator

As mentioned in Sec. 6.1, the signal is coupled into the trap using a helical resonator. This is a common choice in Paul traps, as it allows one to reach high voltages on the electrodes, simplifies the impedance matching of the trap to the rest of the circuit, and filters much of the noise it receives [35]. Next its architecture, working principle, and the simulations of the circuit will be presented.

A helical resonator consists of a small coil (*antenna coil*) inductively coupling the signal into a larger one (*helix* or *helical coil*), which is welded or soldered to a grounded cylindrical shield – as sketched in Fig. 6.2. The other end of the helix and a ground wire are then used to feed the signal to the trap. Intuitively speaking, one expects this device to increase the rms voltage of the input signal (since the inductive coupling is equivalent to a transformer) and to show the signature of a resonance between the inductance of the helix, its self-capacitance, and the capacitive coupling to the shield.

According to [35], such a system can be modelled as the lumped circuit illustrated in Fig. 6.3[1], where all properties can be calculated based on the

[1] The effect of the parasitic properties of the system was taken into account by modifying

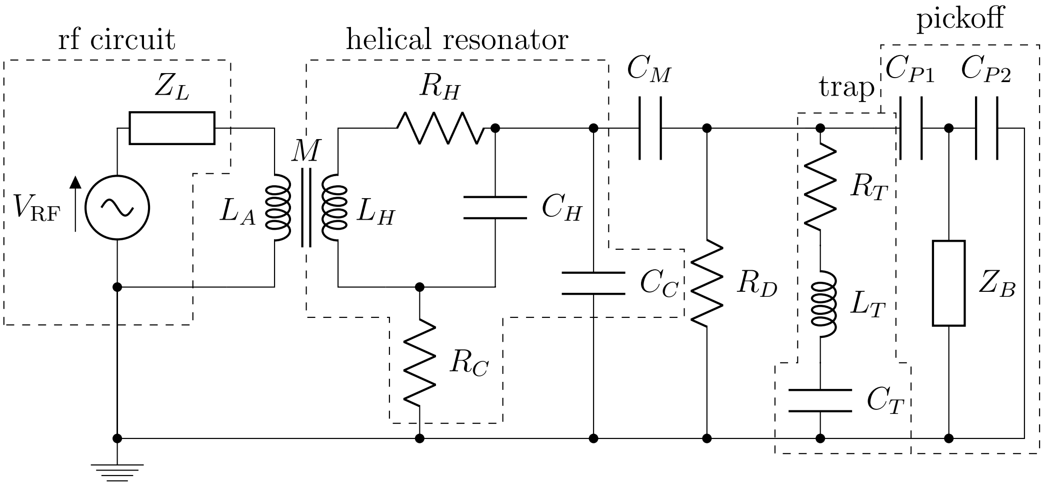

Figure 6.4: Complete model for the helical resonator, the trap, and the pickoff. C_M represents the matching capacitor, R_D the resistor used to drain the static charges, R_T, L_T, and C_T the trap properties, C_{P1} and C_{P2} the capacitors used to sample the signal, and Z_B the impedance of the evaluation board (50 Ω in our case). All other components are listed in Fig. 6.3.

geometry and material of the resonator, and on the rf frequency[2]. Although it looks similar to a RLC circuit, the interplay between the helical resonator, the inductive coupling, and the trap leads to richer behaviour. An exact analytical solution of the circuit can be derived, but it yields very lengthy expressions, from which it is hard to get any useful intuition. An approximate treatment proposed in [35] is unfortunately valid in a slightly different experimental regime from ours, as the assumptions about the inductance and frequency range made there break down in our case. Thus, a simulation was used to predict the behaviour of the system.

Additionally, our apparatus contains a few extra components with respect to that described in Fig. 6.3. Firstly, as the resonator was originally designed [13], it was assumed that the trap could be described as a purely capacitive load. However, when testing the system it turned out that it is best described by a series RLC circuit, and that the inductance L_T is large enough to significantly decrease the resonance frequency of the system. As a consequence, in order to achieve the frequency necessary to trap beryllium, a capacitor between the helix and the trap is needed – referred to as *matching*

the values of the lumped components of our model.

[2] All formulae and a detailed discussion on helical resonators and their design is given in [35].

Parameter	Exp. value	Parameter	Exp. value	Parameter	Exp. value
L_A	50 nH	L_H	75 nH	M	0.1
C_H	0.9 pF	C_C	3.35 pF	C_M	18 pF
R_H	77 mΩ	R_C	152 mΩ	R_D	1 MΩ
R_T	4 mΩ	L_T	100 nH	C_T	27 pF
C_{P1}	0.5 pF	C_{P2}	100 pF	Z_L, Z_B	50 Ω

Table 6.2: Estimated experimental parameters for our system.

capacitor. Due to its presence, static charges that accumulate on the rf electrodes (e.g. due to laser-induced ionisation) cannot flow to ground through the helix. In order to drain them without otherwise changing the circuit behaviour, a large resistor (on the order of 1 MΩ) is placed between the signal going to the trap and ground. We decided to employ a resistor instead of a large inductor (which would be the standard choice for eliminating static charges, since it acts as a low-pass filter on the drained current) because it is placed in a region with strong magnetic noise.

For reasons that will be discussed in Sec.6.3, we decided to insert a capacitive divider in parallel to the trap, in order to sample a small fraction of the signal – the so-called *pickoff*. The simulations indicate that both the large resistor and the pickoff have small effects on the overall behaviour of the system, however it is nonetheless interesting to include them in the final model, which is portrayed in Fig. 6.4.

For the simulation I assumed the input power to be 38 dBm on a 50 Ω transmission line (which corresponds to approximately 18 V rms voltage), and estimated the experimental parameters based on [35] and [13] (obtaining what is listed in Tab. 6.2). The simulation – which was performed with LTSpice – yields the steady-state rms amplitude and phase of the voltage across C_T (which is how the voltage applied to the trap electrodes is modelled) as a function of the input drive frequency assuming an input phase of zero. Its results show a resonance at 111.5 MHz, which is approximately 1.5 MHz lower than what we observe in the lab – a difference which can comfortably be attributed to the uncertainty in our estimates for the lumped circuit model. The voltage amplitude, on the other hand, is significantly lower than what is predicted by [13], which seems to indicate that the power effectively applied to the resonator is higher than what I assumed. Given the linearity of the circuit, however, this seems to be the only relevant difference between the observations and the model.

As a last remark, it is worth mentioning how we use the helical resonator

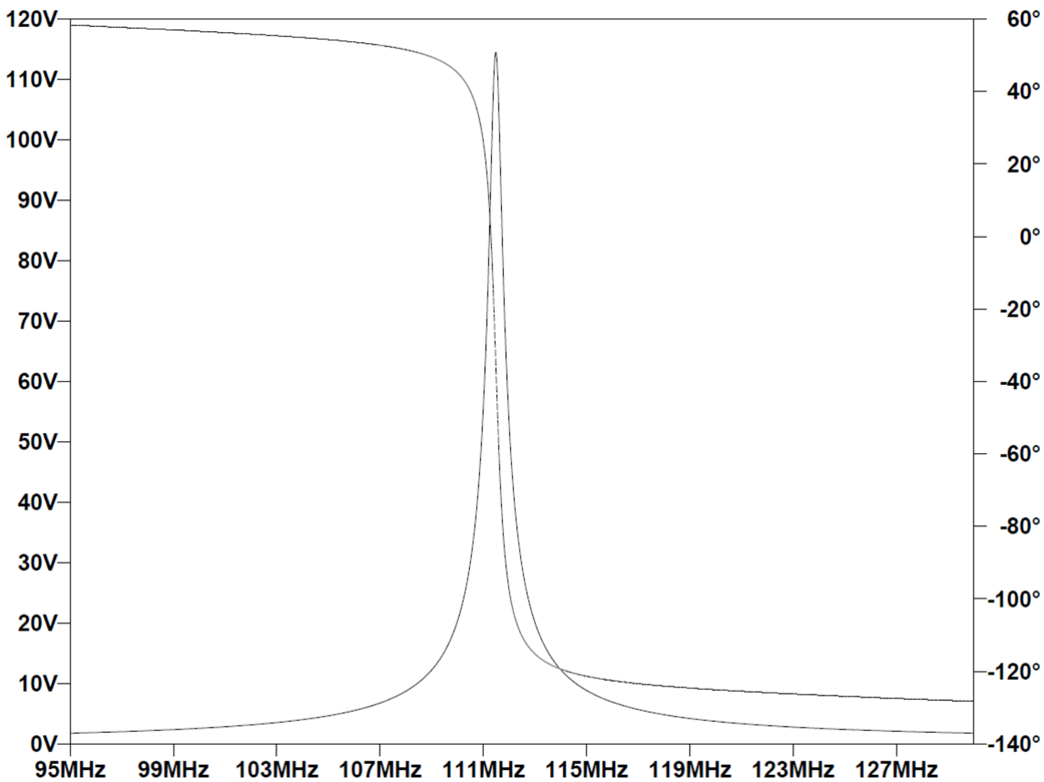

Figure 6.5: Results of the simulation for the circuit. The horizontal axis represents the drive frequency, the peaked curve is the steady-state rms amplitude of the voltage across C_T, and the other curve is the phase of that signal with respect to the drive.

to perform the impedance matching (see [35] for more detail). In order to maximise the fraction of the input power being applied to the electrodes, the total impedance of the circuit including the antenna coil, the resonator, and the trap must match that of the input transmission line. Given the finished apparatus, the parameters which are easiest to modify are the inductance L_A and the inductive coupling M, since the antenna coil is simple to deform by hand, and its position relative to the helix can be changed by moving the cap. One of these parameters would not be enough to change the total impedance sufficiently for our purpose, so we usually modify both by trial and error, until we minimise the reflection – which as mentioned is monitored on a spectrum analyser with the help of the directional coupler shown in Fig. 6.1.

Following from the frequency dependence of the impedances of inductors and capacitors in an ac circuit, the impedance matching (and thus the transmission through the resonator) has a profile in the frequency domain. If only a RLC resonator were connected to the inductive coupling, the maximum-transmission frequency would correspond to the resonance of the resonator. However, since the circuit is rather complex and contains several resonating loops, the voltage applied to the electrodes is given by the convolution of the transmission spectrum and some internal resonance profile. Thus, the frequency for which minimum reflection is reached does not generally correspond to the one yielding maximum voltage. These two frequencies are however close to each other (approximately 100 kHz in our case), since the voltage is ultimately constrained by the transmission through the resonator.

6.3 The Feedback System

The feedback scheme applied in order to stabilise the rf amplitude is similar to the one used in [36]: a small fraction of the signal is sampled and fed to an evaluation board (Analog Devices ADL5511), which outputs a dc voltage proportional to its RMS amplitude. The output of the board is then given as an error signal to a PID controller (Newport New Focus LB1005), which feeds back on the signal by changing the dc-coupled voltage applied to the IF port of a mixer. The devices are listed in Tab. 6.1. Initially we used a different PID controller (SRS SIM960), to which we might return depending on the results yielded by the current one – as it is slower, but has a stabler setpoint.

A critical point when designing a feedback system is the choice of where to sample the signal [36]. Indeed, it should be picked off as close to the trap electrodes as possible – otherwise it cannot take into account the noise introduced by the following components in the circuit – but at the same time

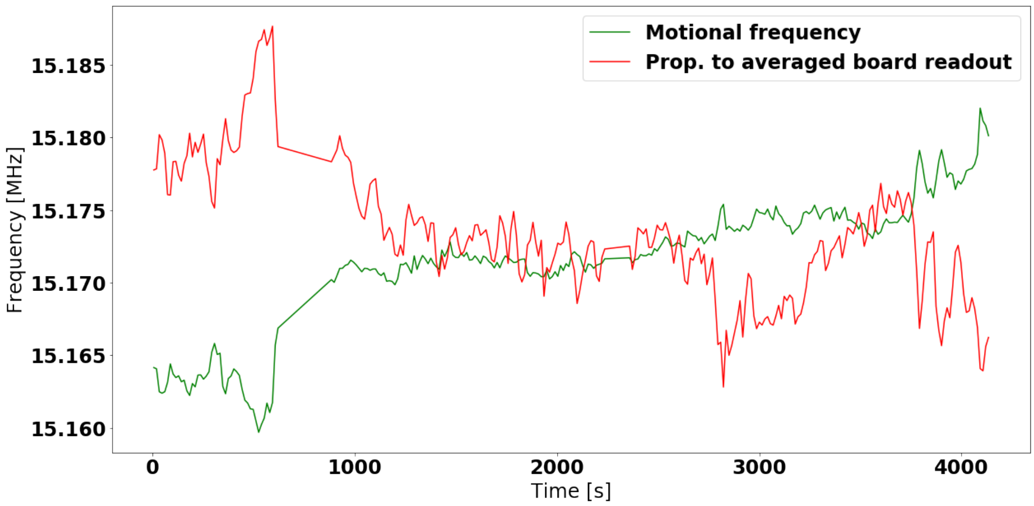

Figure 6.6: Comparison between the measured radial motional frequency of beryllium (green) and the evaluation board readout (red) as a function of time. Here the signal is sampled before the resonator.

it should not influence the behaviour of the resonator too strongly. During this thesis two possibilities were tested, as described in the following.

6.3.1 Sampling Before the Resonator

The first (and most straightforward) attempt we made to sample the signal was to insert an additional coupler into the rf box, right before the output going to the resonator, which sent approximately 1% of the signal to the evaluation board. This scheme is not depicted in any of the figures in this thesis, because it was not our final choice.

To assess the reliability of the read-out signal (given by the correlation of the signal and the motional frequency), we kept track of the motional frequency as a function of time (with repeated sideband or tickle experiments), while also measuring the output of the evaluation board. Even though this method has poor time resolution (as the experiments we use to determine the motional frequency last at least a few seconds each), it gives us a useful indication of the correlation between the motional frequency and the eval board readout.

As shown in Fig. 6.6, the two data sets do not seem correlated. Our conclusion was that the resonator introduces some strong drift, which makes the signal picked off beforehand entirely unreliable.

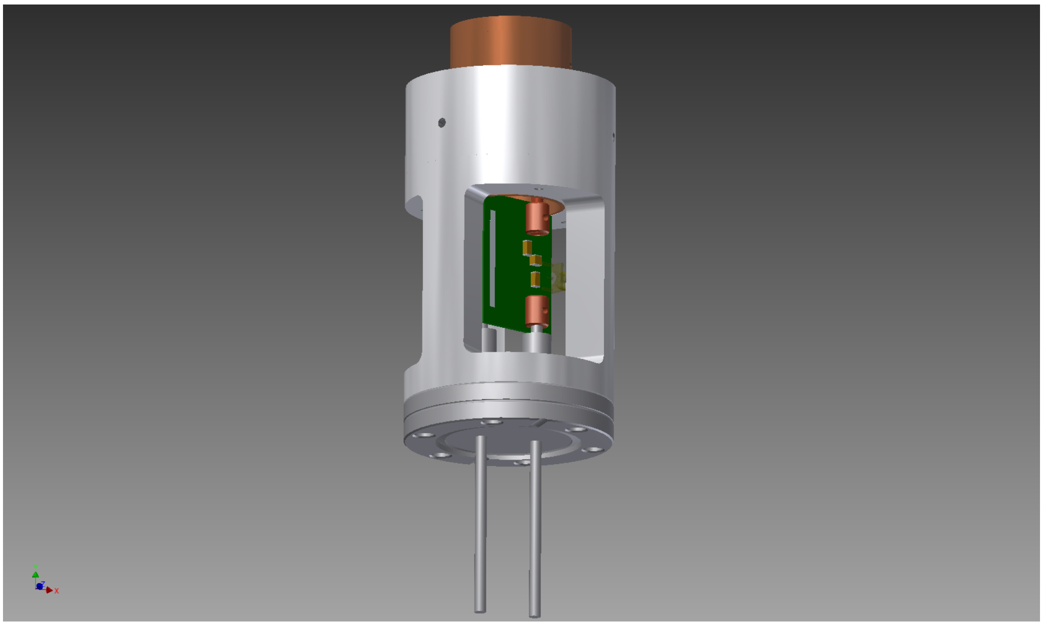

Figure 6.7: Layout of the new resonator base with the PCB. The grey component at the bottom is screwed on top of the vacuum chamber and feeds the signal to the trap, the copper part at the top is the cap, and the large aluminium piece in the middle is the base sustaining the resonator (which is barely visible in this image).

6.3.2 Sampling After the Resonator

The latest point in the circuit before the vacuum chamber one can sample the signal from is between the helical resonator and the contacts feeding the signal to the trap. We thus decided to insert a pickoff there (consisting of a capacitive divider [36]), as sketched in Fig. 6.1.

This approach required some larger adaptations to the apparatus than what is presented in Sec. 6.3.1, but it was still not too invasive – it did not require opening or modifying the vacuum chamber. In order to apply these changes, we decided to fit the matching capacitor and the pickoff on a printed-circuit board (PCB, which is going to be discussed in Sec. 6.4). This can be screwed to the resonator on one side and to the trap on the other thanks to some copper contacts that are soldered on top of it, as shown in Fig. 6.7.

The correlation of this signal to the motional frequency was tested with the same experiment as in Sec. 6.3.1 and the results are shown in Fig. 6.8.

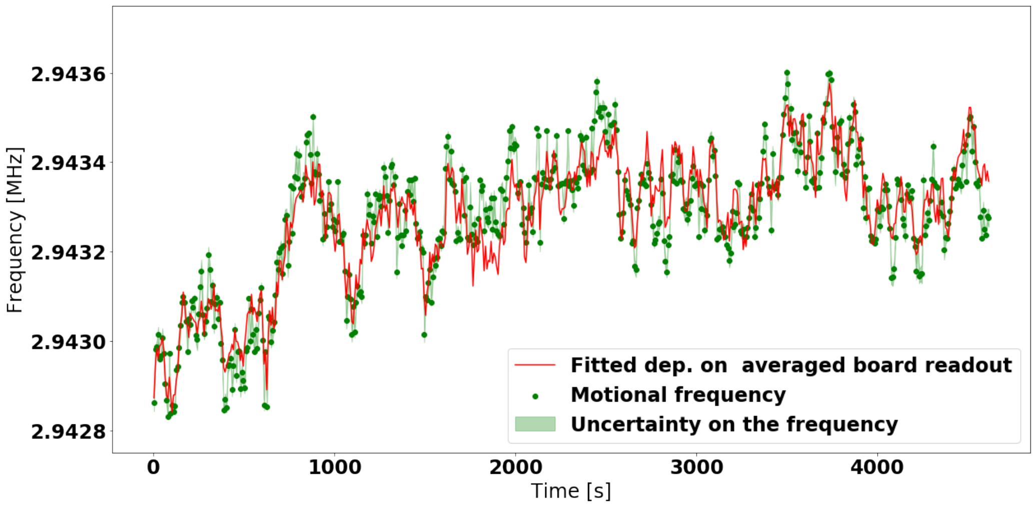

Figure 6.8: Comparison between the measured radial motional frequency of calcium and the evaluation board readout as a function of time. Here the signal is sampled after the resonator. Qualitative comparison shows clear correlation between the two data sets. This data was taken while locking, which explains the higher stability than the one observed in Fig. 6.6.

In this case it was possible to use Eq. (2.34) to fit the data to the function

$$\omega_x(V_{board}) = \sqrt{a\, V_{board}^2 - b}, \tag{6.1}$$

which connects the eval board readout V_{board} to the motional frequency ω_x, where $a, b \in \mathbb{R}_+$ are the fit parameters. The correlation between ω_x and V_{board} is much stronger than what can be achieved by sampling the signal before the resonator. The discrepancies between the two data sets in Fig. 6.8 can be due to many factors, among which some additional noise introduced after the pickoff, the noise on the line transmitting the board readout to the multimeter we used to record its output (which is a ten-meter coaxial cable in a rather noisy environment), and the poor resolution of the frequency scans.

It is however important to bear in mind that this result alone is not sufficient to prove that this signal can be used to implement a serviceable feedback. Indeed, more complete information can be gained by applying the feedback to the system and testing its effect on both slow and fast noise (according to Sec. 4.4.2) as it is going to be presented in Sec. 6.5.

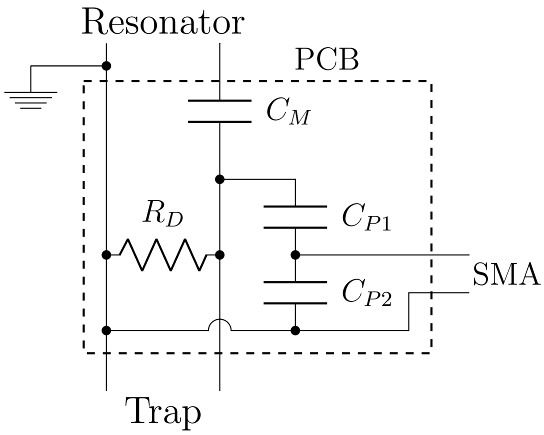

Figure 6.9: Circuit diagram of the PCB. The signal sampled by the the pickoff is output through an SMA port.

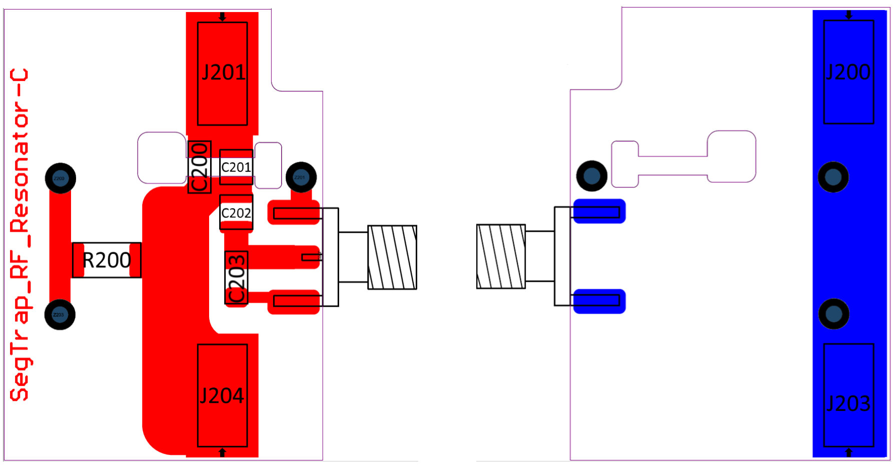

Figure 6.10: Layout of the top (left) and bottom (right) of the PCB (designed with Altium Designer). The red and blue areas represent the tracks printed respectively on the top and on the bottom, the thin purple lines are the physical edges of the PCB, and the circles are plated vias. The components C200 and C201 are two alternatives for C_M, C202 and C203 are C_{P1} and C_{P2}, respectively, R200 is R_D, J200,J201,J203,J204 are the solder pads for the contacts, and J202 is a SMA connector.

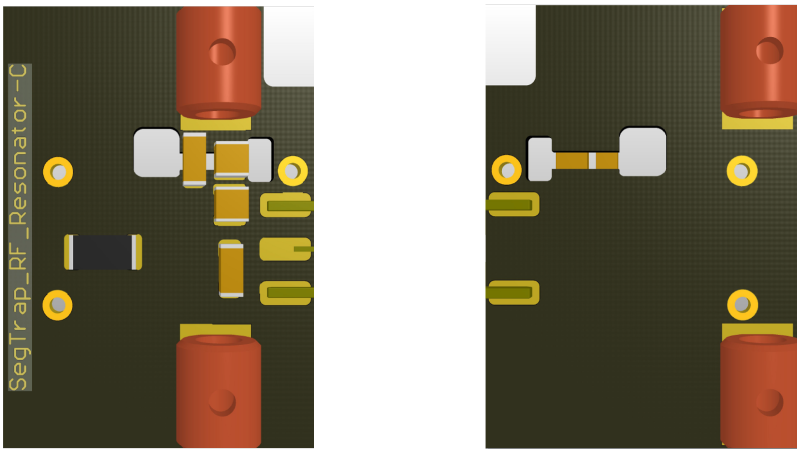

Figure 6.11: Top (left) and bottom (right) view of the PCB (designed with Altium Designer). The copper contacts are hollow cylinders in which the wires from the resonator and the trap can be tightened with a screw (the screw holes are visible in the image). The two top capacitors are two alternatives for C_M, thus only one of them is going to be mounted on the PCB.

6.4 The Printed-Circuit Board

In order to insert the capacitive divider after the resonator, a PCB is a very convenient choice, as it can be fit into the existing apparatus with few adaptations (we only needed to redesign the aluminium base supporting the resonator), it allows us to easily substitute the components (which was problematic with the previously adopted solution), and it makes the apparatus more flexible for future adaptations – as many functionalities could be added just by designing a new PCB. Nevertheless, some special care must be taken in the design stage, since this PCB is used in a rather unusual regime, namely radio frequency and high voltage.

Let me first mention two issues that we do not need to worry about, that is to say the resistivity of the tracks and the impedance matching along the circuit. Since at 110 MHz the skin depth of copper is approximately 6 μm – i.e. 90% of the current flows within 14 μm from the surface – and the standard track thickness is 35 μm, it is enough to draw tracks several millimetres wide to have roughly the same conductivity in the PCB as in the copper rods and coaxial cables that are used in the rest of the circuit. Regarding the impedance matching, it is only worth considering the circuit as a transmission line when its length is comparable to or larger than the quarter wavelength of the signal, which is not the case here [37] – as the length of the tracks is a few centimetres, whereas the wavelength of a 110 MHz signal in copper is approximately 1.6 m – thus we can neglect the local impedance of the circuit on the PCB. Note that this does not mean that we can neglect the impedance matching to external devices and transmission lines, which is given by the interplay between the circuit on the PCB, the trap, and the resonator.

6.4.1 The PCB Material

Due to the size of the tracks being much smaller than the quarter wavelength of the signal, we can neglect the antenna-like radiative losses from the circuit. However, one must take into account that there is an oscillating electric field around the tracks, which polarises the dielectric substrate. Thus, depending on the material, some energy is dissipated by means of resistive losses, giving rise to *dielectric losses*. To minimise this effect, we use a low-loss material for the PCB (Rogers 4350B), which has a much lower loss tangent than the standard FR-4 dielectric. Unfortunately we cannot quantify this difference precisely, as no numeric values are given by the PCB manufacturers for our frequency range (with lower voltages dielectric losses become relevant in the GHz regime) and we did not test the two materials with equivalent designs.

Given the frequency and length scale of interest, the field around the lines can be assumed to be distributed as in electrostatics, leading to some intuition about where the losses are most significant, which can be used to further reduce them. First of all, it is clear that any capacitive coupling between signal and ground causes a strong field in the region between the two, therefore any overlap between their tracks must be avoided. Furthermore, if there is a strong voltage amplitude or phase difference across a component, one might consider drilling some of the dielectric away.

The first version of the PCB was made of standard FR-4 dielectric and had one side completely covered by a ground plane (i.e. total overlap between the tracks and ground). When first testing it we noticed that most power was being dissipated and that the situation was worsening with time. After a few tens of minutes the material around the first centimetre of the track had darkened due to the heat produced. In the following weeks we observed that manually removing the ground plane from under the tracks, using a thinner layer of dielectric, and removing the material around the matching capacitor helped, which made it clear that the dielectric losses are a major issue.

Based on these guidelines, we obtained the final design depicted in Fig. 6.10 and Fig. 6.11, where the ground of the SMA connector is connected to the system ground through a mid-air cable in order to minimise the capacitive

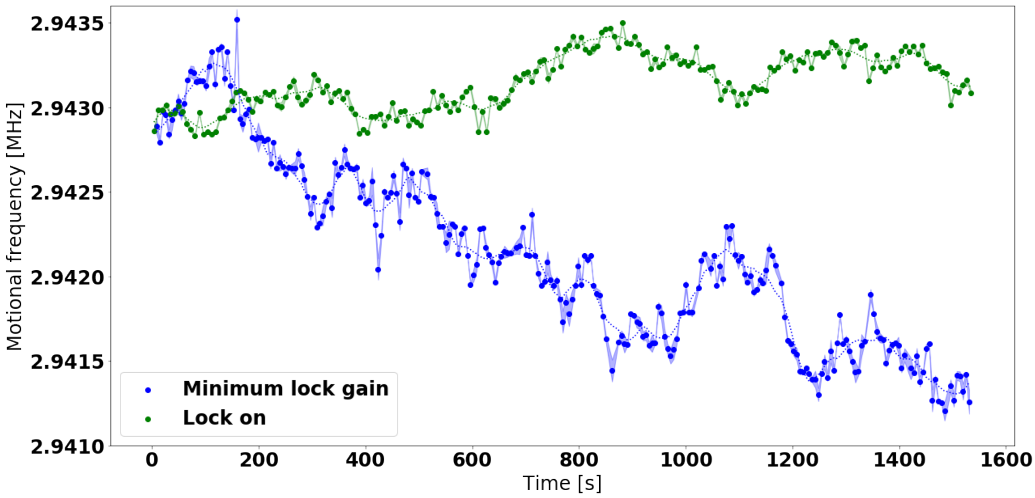

Figure 6.12: Comparison between the time evolution of the motional frequency while applying the lock and maximising the motional frequency (green) and with minimum lock gain and minimising the reflection (blue). The blue data are shifted by 0.043 MHz in order to be in the same region of the plot as the green ones.

coupling to the signal, and the PCB material is cut away around C_M, which is a region in which we observed experimentally strong losses.

6.4.2 The Capacitors

As mentioned above, where a capacitive coupling is present, the dielectric loss due to the polarisation of the medium present in the region can become problematic. This is also true inside capacitors, which must therefore be chosen accordingly. Here, the problem is again that we operate them in an unusual regime, therefore the relevant specifications in the relevant frequency range are not given by the manufacturers. In particular, while testing one of the temporary versions of the PCB, we concluded that the Vishay Vitramon VJ1111D180JXRAJ capacitor dissipates less power than the other option we tried (AVX 1808HA180JAT1A), and is therefore more adequate to be used as C_M, which is subject to strong fields.

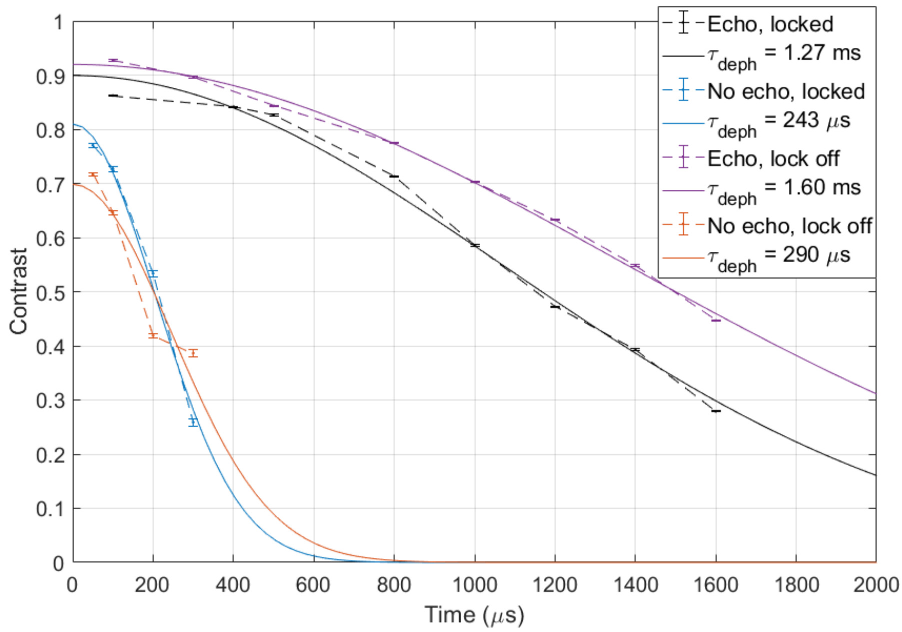

Figure 6.13: Contrast of the motional Ramsey experiment as a function of the waiting time with different settings, namely with and without locking and with and without the motional echo. The solid lines represent the fitted Gaussian decay with characteristic dephasing time τ_{deph}. Image credit: Karan Mehta.

6.5 Applying the Feedback

As mentioned at the beginning of this chapter, the sampled rf signal is processed by an evaluation board (Analog Devices ADL5511), which sends a dc signal to a fast PID controller (Newport New Focus LB1005). The PID controller then changes the voltage applied to the IF port of a mixer, thereby modulating the amplitude of the rf signal earlier in the rf chain, as shown in Fig. 6.1.

As explained in Sec. 6.2, the frequency where the reflected power from the helical resonator is minimised is approximately 100 kHz below that at which the voltage amplitude on the trap electrodes (and therefore the radial motional frequency of the ions) is maximised. Thus, setting the rf frequency to minimise the reflected power yields a value slightly detuned from the maximum of the curve shown in Fig. 6.5, making the motional frequency more sensitive to oscillations in the system parameters which modify the electronic properties of its components and thereby shift the resonance profile (e.g. thermal variations). It may therefore be beneficial to set the rf frequency such that the radial motional frequencies are maximised. Note that this also reduces the effect of the frequency noise generated after the pickoff, which cannot be corrected by the feedback system.

Fig. 6.12 shows the results of tuning the rf frequency based on the radial mode frequency and applying the feedback versus basing on the reflection and tweaking the PID parameters to minimum. Even though the improvement is clear, it is unclear how much of the radial mode frequency drift is caused by frequency noise versus the different lock settings; this requires further investigation.

The effects of the feedback can be further characterised using the motional Ramsey experiments with and without motional echo, as shown in Fig. 6.13. Following from the discussion in Sec. 4.4.2, we conclude that the slow drifts dominate the motional dephasing process, and that the lock seems to be unable to prevent them. The fact that the motional coherence time is smaller when locking suggests that there is some slow noise in the feedback system.

The fast noise, on the other hand, seems to be low enough to allow for more than a millisecond motional coherence also without locking, which is enough to drive high-fidelity MS gates. The behaviour of the contrast in the experiments with motional echo is not completely consistent with Eq. (4.38), which predicts an exponential decay. This discrepancy can however be due to many factors, such as the time needed to apply the echo pulses being longer than 100 μs and potentially the noise on timescales close to the Ramsey wait time.

6.6 Next Steps

From the previous section it is clear that slow radial-mode frequency drift is currently the dominant effect limiting the radial mode stability and coherence. To reduce drift, there are several possibilities that can be tested. In the following I list the ones we plan to try out in the near future.

First of all, we observed that the motional frequency, the evaluation board readout, and their correlation can be influenced by moving some cables, which indicates that significant noise is picked up in several parts of the circuit. Once the most critical points (i.e. the cables that influence the signal more strongly) are identified, it should be straightforward to reduce this problem considerably – for example by adding rf chokes and replacing or re-arranging cables.

Secondly, the quality of the lock also strongly depends on the stability of the voltage reference used by the PID controller for its setpoint. Since the fast noise is not currently the limiting factor, it may be advantageous to switch back to the slower PID controller (SRS SIM960), which has a lower control bandwidth than the current one, and possibly a stabler setpoint. As an alternative to this, or as an additional measure, we could stabilise the temperature of the PID controller, which is currently placed on top of the rf box which dissipates heat in an uncontrolled way. In the same spirit, both the supply voltage and the temperature of the evaluation board could be stabilised.

Thirdly, since the output of the evaluation board covers a small fraction of the input range of the PID controller, one could think about amplifying it in order to improve the resolution of the stabilisation. It is however important to carefully choose an amplifier that does not introduce significant noise.

Chapter 7

Summary and Outlook

In this thesis I have presented our theoretical and experimental efforts towards the realisation of transport Mølmer Sørensen gates. As argued in Chap. 5, such gates can be relevant in that they represent the translation of a fundamental building block of quantum computation to a scalable working principle. In addition to this, I introduced the relevant physics and the relevant parts of the apparatus, such that a reader with a background in quantum information processing should be able to follow the whole text without difficulty.

The theoretical and computational study of the gate was aimed at identifying the main sources of gate infidelity, in order to direct our experimental efforts. From the discussions in Chap. 4 and 5 it is clear that the most problematic error sources are the rf amplitude instability, the AC Stark shift, and the Doppler shift. Due to time constraints, the first was the one on which we focussed our efforts so far, whereas a solution to the other effects was proposed and will be further investigated in the future.

As described in Chap. 6, the work on the rf stability led to several modifications of the apparatus, the most significant one being the addition of a printed circuit board, which enables us to sample the rf signal after the helical resonator and enhances the flexibility of the setup for future modifications (such as using rf signals to drive transitions between the calcium S states).

The rf amplitude stabilisation turned out to be more challenging than we originally expected, and is currently under active development. In particular, our most recent observations suggest that the slow drifts in the rf circuit and in the feedback system are the main limitation to the motional phase coherence of the ions, and are therefore being investigated. Given the complexity of the apparatus, identifying the sources of these drifts is not trivial, and is being done by trial and error.

Once we stabilise the rf amplitude sufficiently to get the coherence time to the desired level (see Sec. 4.4.2), it will be necessary to investigate the feasibility of the mutual compensation of the AC Stark and Doppler shift proposed in Sec. 5.4.4. Being the new Raman beam path ready to operate, this might be the last step towards the realisation of high-fidelity transport Mølmer Sørensen gates.

Bibliography

[1] Peter W. Shor. Polynomial-Time Algorithms for Prime Factorization and Discrete Logarithms on a Quantum Computer. *SIAM Journal on Computing*, 26(5):1484–1509, October 1997. arXiv: quant-ph/9508027.

[2] David P. DiVincenzo. The Physical Implementation of Quantum Computation. *Fortschritte der Physik*, 48(9-11):771–783, September 2000.

[3] D.J. Wineland, C. Monroe, W.M. Itano, D. Leibfried, B.E. King, and D.M. Meekhof. Experimental issues in coherent quantum-state manipulation of trapped atomic ions. *Journal of Research of the National Institute of Standards and Technology*, 103(3):259, May 1998.

[4] Roee Ozeri. The trapped-ion qubit tool box. *Contemporary Physics*, 52(6):531–550, November 2011.

[5] Scott Aaronson and Lijie Chen. Complexity-Theoretic Foundations of Quantum Supremacy Experiments. *arXiv:1612.05903 [quant-ph]*, December 2016. arXiv: 1612.05903.

[6] D. Leibfried, E. Knill, C. Ospelkaus, and D. J. Wineland. Transport quantum logic gates for trapped ions. *Physical Review A*, 76(3), September 2007.

[7] Ludwig E. de Clercq, Hsiang-Yu Lo, Matteo Marinelli, David Nadlinger, Robin Oswald, Vlad Negnevitsky, Daniel Kienzler, Ben Keitch, and Jonathan P. Home. Parallel Transport Quantum Logic Gates with Trapped Ions. *Physical Review Letters*, 116(8), February 2016.

[8] Wolfgang Paul. Electromagnetic traps for charged and neutral particles. *Reviews of Modern Physics*, 62(3):531–540, July 1990.

[9] Florian Leupold. *Bang-bang Control of a Trapped-Ion Oscillator*. PhD Thesis, ETH, Zurich, 2015.

[10] Roy J. Glauber. *Quantum Theory of Optical Coherence*. Wiley-VCH Verlag GmbH & Co. KGaA, Weinheim, Germany, December 2006.

[11] D. Leibfried, R. Blatt, C. Monroe, and D. Wineland. Quantum dynamics of single trapped ions. *Reviews of Modern Physics*, 75(1):281–324, March 2003.

[12] Hsiang-Yu Lo. *Creation of Squeezed Schroedinger's Cat States in a Mixed-Species Ion Trap*. PhD Thesis, ETH, Zurich, 2015.

[13] D. Kienzler, H.-Y. Lo, B. Keitch, L. de Clercq, F. Leupold, F. Lindenfelser, M. Marinelli, V. Negnevitsky, and J. P. Home. Quantum harmonic oscillator state synthesis by reservoir engineering. *Science*, 347(6217):53–56, January 2015.

[14] Robin Oswald. Velocity Control of Trapped Ions for Transport Quantum Logic Gates. Master's thesis, ETH, Zurich, November 2015.

[15] D. Kielpinski, C. Monroe, and D. J. Wineland. Architecture for a large-scale ion-trap quantum computer. *Nature*, 417(6890):709–711, June 2002.

[16] Serge Haroche and Jean-Michel Raimond. *Exploring the Quantum: Atoms, Cavities, and Photons*. Oxford University Press, August 2006.

[17] Jonathan P. Home and Joseba Alonso Otamendi. Cavity QED and Ion Trap Physics, Lecture Notes, July 2015.

[18] Roy J. Glauber. Coherent and Incoherent States of the Radiation Field. *Physical Review*, 131(6):2766–2788, September 1963.

[19] S. Blanes, F. Casas, J. A. Oteo, and J. Ros. The Magnus expansion and some of its applications. *Physics Reports*, 470(5-6):151–238, January 2009. arXiv: 0810.5488.

[20] D. J. Wineland, M. Barrett, J. Britton, J. Chiaverini, B. DeMarco, W. M. Itano, B. Jelenković, C. Langer, D. Leibfried, V. Meyer, T. Rosenband, and T. Schätz. Quantum information processing with trapped ions. *Philosophical Transactions of the Royal Society A: Mathematical, Physical and Engineering Sciences*, 361(1808):1349–1361, July 2003. arXiv: quant-ph/0212079.

[21] C. A. Sackett, D. Kielpinski, B. E. King, C. Langer, V. Meyer, C. J. Myatt, M. Rowe, Q. A. Turchette, W. M. Itano, D. J. Wineland,

and C. Monroe. Experimental entanglement of four particles. *Nature*, 404(6775):256–259, March 2000.

[22] D. Leibfried, B. DeMarco, V. Meyer, D. Lucas, M. Barrett, J. Britton, W. M. Itano, B. Jelenković, C. Langer, T. Rosenband, and D. J. Wineland. Experimental demonstration of a robust, high-fidelity geometric two ion-qubit phase gate. *Nature*, 422(6930):412–415, March 2003.

[23] P. J. Lee, K.-A. Brickman, L. Deslauriers, P. C. Haljan, L.-M. Duan, and C. Monroe. Phase control of trapped ion quantum gates. *Journal of Optics B: Quantum and Semiclassical Optics*, 7(10):S371–S383, October 2005.

[24] A. M. Steane, G. Imreh, J. P. Home, and D. Leibfried. Pulsed force sequences for fast phase-insensitive quantum gates in trapped ions. *New Journal of Physics*, 16(5):053049, May 2014.

[25] Klaus Mølmer and Anders Sørensen. Multiparticle Entanglement of Hot Trapped Ions. *Physical Review Letters*, 82(9):1835–1838, March 1999.

[26] Anders Sørensen and Klaus Mølmer. Quantum Computation with Ions in Thermal Motion. *Physical Review Letters*, 82(9):1971–1974, March 1999.

[27] Anders Sørensen and Klaus Mølmer. Entanglement and quantum computation with ions in thermal motion. *Physical Review A*, 62(2), July 2000.

[28] P. C. Haljan, K.-A. Brickman, L. Deslauriers, P. J. Lee, and C. Monroe. Spin-Dependent Forces on Trapped Ions for Phase-Stable Quantum Gates and Entangled States of Spin and Motion. *Physical Review Letters*, 94(15), April 2005.

[29] Christa Flühmann, Thanh Long Nguyen, Matteo Marinelli, Vlad Negnevitsky, Karan Mehta, and Jonathan Home. Encoding a qubit in a trapped-ion mechanical oscillator. *arXiv:1807.01033 [physics, physics:quant-ph]*, July 2018. arXiv: 1807.01033.

[30] Christopher J. Ballance. *High-Fidelity Quantum Logic in Ca+*. Springer Theses. Springer International Publishing, Cham, 2017.

[31] J.R. Johansson, P.D. Nation, and Franco Nori. QuTiP 2: A Python framework for the dynamics of open quantum systems. *Computer Physics Communications*, 184(4):1234–1240, April 2013.

[32] Christopher E Langer. *High Fidelity Quantum Information Processing with Trapped Ions*. PhD Thesis, NIST, Boulder, Colorado, USA, 2006.

[33] Jonathan P. Home. *Entanglement of Two Trapped-Ion Spin Qubits*. PhD Thesis, Linacre College, Oxford, 2006.

[34] L. E. de Clercq, R. Oswald, C. Flühmann, B. Keitch, D. Kienzler, H. Y. Lo, M. Marinelli, D. Nadlinger, V. Negnevitsky, and J. P. Home. Estimation of a general time-dependent Hamiltonian for a single qubit. *Nature Communications*, 7:11218, April 2016.

[35] J. D. Siverns, L. R. Simkins, S. Weidt, and W. K. Hensinger. On the application of radio frequency voltages to ion traps via helical resonators. *Applied Physics B*, 107(4):921–934, June 2012.

[36] K. G. Johnson, J. D. Wong-Campos, A. Restelli, K. A. Landsman, B. Neyenhuis, J. Mizrahi, and C. Monroe. Active Stabilization of Ion Trap Radiofrequency Potentials. *Review of Scientific Instruments*, 87(5):053110, May 2016. arXiv: 1603.05492.

[37] John Coonrod. Circuit Materials and High-Frequency Losses of PCBs. page 6.